

## ARTICLE OPEN



# Targeting HIV Env immunogens to B cell follicles in nonhuman primates through immune complex or protein nanoparticle formulations

Jacob T. Martin<sup>1,2,16</sup>, Christopher A. Cottrell<sup>1,2,3,16</sup>, Aleksandar Antanasijevic<sup>2,3,16</sup>, Diane G. Carnathan<sup>2,4,5</sup>, Benjamin J. Cossette<sup>1,2</sup>, Chiamaka A. Enemu<sup>4,5</sup>, Etse H. Gebru<sup>4,5</sup>, Yury Choe<sup>4,5</sup>, Federico Viviano<sup>4,5</sup>, Stephanie Fischinger<sup>6,7</sup>, Talar Tokatlian<sup>1,2</sup>, Kimberly M. Cirelli<sup>2,8</sup>, George Ueda<sup>9,10</sup>, Jeffrey Copps<sup>10</sup>, Torben Schiffner<sup>2,11</sup>, Sergey Menis<sup>2,11</sup>, Galit Alter<sup>10</sup>, William R. Schief<sup>10,11</sup>, Shane Crotty<sup>2,8,12</sup>, Neil P. King<sup>9,10</sup>, David Baker<sup>9,10,13</sup>, Guido Silvestri<sup>2,4,5</sup>, Andrew B. Ward<sup>2,3,11</sup>✉ and Darrell J. Irvine<sup>1,2,6,13,14,15</sup>✉

Following immunization, high-affinity antibody responses develop within germinal centers (GCs), specialized sites within follicles of the lymph node (LN) where B cells proliferate and undergo somatic hypermutation. Antigen availability within GCs is important, as B cells must acquire and present antigen to follicular helper T cells to drive this process. However, recombinant protein immunogens such as soluble human immunodeficiency virus (HIV) envelope (Env) trimers do not efficiently accumulate in follicles following traditional immunization. Here, we demonstrate two strategies to concentrate HIV Env immunogens in follicles, via the formation of immune complexes (ICs) or by employing self-assembling protein nanoparticles for multivalent display of Env antigens. Using rhesus macaques, we show that within a few days following immunization, free trimers were present in a diffuse pattern in draining LNs, while trimer ICs and Env nanoparticles accumulated in B cell follicles. Whole LN imaging strikingly revealed that ICs and trimer nanoparticles concentrated in as many as 500 follicles in a single LN within two days after immunization. Imaging of LNs collected seven days postimmunization showed that Env nanoparticles persisted on follicular dendritic cells in the light zone of nascent GCs. These findings suggest that the form of antigen administered in vaccination can dramatically impact localization in lymphoid tissues and provides a new rationale for the enhanced immune responses observed following immunization with ICs or nanoparticles.

npj Vaccines (2020)5:72; <https://doi.org/10.1038/s41541-020-00223-1>

## INTRODUCTION

The development of immunogens/immunization regimens capable of eliciting broadly neutralizing antibodies (bNAbs) that can recognize diverse viral strains is thought to be an important approach to achieve an effective human immunodeficiency virus (HIV) vaccine<sup>1,2</sup>. The sole target for neutralizing antibodies on the virus surface is the envelope (Env) protein, a homotrimer consisting of three copies of gp120 and gp41 subunits that are associated by non-covalent interactions. Methods enabling the production of stable recombinant trimer immunogens based on the ectodomain of Env have catalyzed recent HIV vaccine efforts<sup>3–10</sup>. However, optimizing immunization strategies to promote high-affinity antibody responses against trimer immunogens remains an important goal. B cell affinity maturation occurs in germinal centers (GCs) formed within B cell follicles in lymph nodes (LNs), and the availability of antigen to B cells within GCs plays a critical role in regulating the outcome of immunization<sup>11–13</sup>. Hence, the efficient trafficking of Env trimer immunogens to follicles following

immunization is likely essential to promote optimal humoral responses to HIV.

Upon immunization, soluble immunogens are rapidly bound by antibodies present in the tissue, forming immune complexes (ICs) that can subsequently traffic into lymphatic vessels and downstream draining LNs. In antigen-naïve animals, IC formation can be mediated by natural pentameric IgM (nIgM) that binds antigen with low affinity but moderate to high avidity<sup>14,15</sup>. Antigen–antibody ICs are subsequently opsonized by complement, ultimately resulting in the covalent attachment of the complement protein C3d<sup>14,15</sup>. As the IC–C3d complexes enter the draining LN, they are captured by subcapsular sinus (SCS) macrophages via complement receptors and are transported across the SCS floor into the B cell follicle<sup>16–18</sup>. Non-antigen-specific, naïve B cells capture IC–C3d complexes from the basolateral surface of SCS macrophages using complement receptor 2 and deposit them onto the surface of follicular dendritic cells (FDCs), where they are subsequently available to participate in

<sup>1</sup>Koch Institute for Integrative Cancer Research, Massachusetts Institute of Technology, Cambridge, MA 02139, USA. <sup>2</sup>Center for HIV/AIDS Vaccine Development, The Scripps Research Institute, La Jolla, CA 92037, USA. <sup>3</sup>Department of Integrative Structural and Computational Biology, The Scripps Research Institute, La Jolla, CA 92037, USA. <sup>4</sup>Yerkes National Primate Research Center, Emory University, Atlanta, GA 30322, USA. <sup>5</sup>Emory Vaccine Center, Emory University School of Medicine, Atlanta, GA 30322, USA. <sup>6</sup>Ragon Institute of Massachusetts General Hospital, Massachusetts Institute of Technology and Harvard University, Cambridge, MA 02139, USA. <sup>7</sup>University of Duisburg-Essen, 47057 Essen, Germany. <sup>8</sup>Center for Infectious Disease and Vaccine Research, La Jolla Institute for Immunology (LJI), La Jolla, CA 92037, USA. <sup>9</sup>Department of Biochemistry, University of Washington, Seattle, WA 98195, USA. <sup>10</sup>Institute for Protein Design, University of Washington, Seattle, WA 98195, USA. <sup>11</sup>International AIDS Vaccine Initiative Neutralizing Antibody Center, The Scripps Research Institute, La Jolla, CA 92037, USA. <sup>12</sup>Department of Medicine, Division of Infectious Diseases and Global Public Health, University of California, San Diego, La Jolla, CA 92037, USA. <sup>13</sup>Howard Hughes Medical Institute, Chevy Chase, MD 20815, USA. <sup>14</sup>Department of Biological Engineering, Massachusetts Institute of Technology, Cambridge, MA 02139, USA. <sup>15</sup>Department of Materials Science and Engineering, Massachusetts Institute of Technology, Cambridge, MA 02139, USA. <sup>16</sup>These authors contributed equally: Jacob T. Martin, Christopher A. Cottrell, Aleksandar Antanasijevic. ✉email: [andrew@scripps.edu](mailto:andrew@scripps.edu); [djirvine@mit.edu](mailto:djirvine@mit.edu)

the GC reaction<sup>17</sup>. FDCs serve as antigen depots that are capable of storing and displaying antigen for months<sup>19</sup>.

Soluble HIV Env immunogens do not follow the above canonical pathway for entering the B cell follicle<sup>20</sup>. Most likely due to the high level of glycosylation and the low capacity to form avidity-enhanced interactions, soluble Env trimers do not efficiently bind nIgM or activate complement<sup>21</sup>. Instead, they enter the LN as free antigens and are captured by interfollicular channel (IFC) macrophages via cell surface SIGN-R1 receptors<sup>20</sup>. Antigen-specific naive B cells have an opportunity to interact with captured antigen on the surface of IFC macrophages as the B cells exit the circulatory system on their way to the B cell follicle. Additionally, IFC macrophages extend antigen-bearing cellular processes into the B cell follicle where antigen-specific follicular B cells can capture antigen along the edge of the follicle<sup>20</sup>. This alternative antigen trafficking pathway allows for the initial activation of B cells, but does not provide additional antigen needed for repeated cycles of the GC reaction<sup>20</sup>. Presumably, the initial activation of naive B cells results in a production of short-lived plasmablasts, which secrete antibodies capable of forming ICs with soluble Env immunogens that can eventually be deposited on FDCs<sup>22</sup>. This delay in Env immunogen trafficking to FDCs could potentially result in a loss of antigenic integrity, due to degradation of the immunogen by endogenous proteases, promoting dominance of antibody responses focused on non-neutralizing epitopes<sup>21,23</sup>.

These issues motivate the exploration of methods to promote rapid delivery of Env immunogens to follicles, such as alternative approaches to engage the natural complement-mediated pathway for delivery of ICs to follicles. Fusion of antigens with multiple copies of recombinant C3 has been shown to enhance humoral immunity<sup>24</sup>, but this strategy has not been widely applied and may be difficult to implement generally. Another approach is to form synthetic ICs with recombinant monoclonal antibodies<sup>25–28</sup>. Immunization with ICs in animal models has been shown in some cases to enhance immunoglobulin G (IgG) titers and duration, and to affect which epitopes are targeted<sup>27–30</sup>. Early-stage clinical trials of IC immunization have shown this approach to also be safe<sup>31,32</sup>. Passive administration of bnAbs against HIV Env is now being investigated in numerous clinical trials with good safety profiles reported for a variety of bnAbs<sup>33–35</sup>, suggesting a pathway for rapid clinical translation of IC immunization against HIV.

Recently, we discovered another approach for promoting complement decoration of immunogens that is independent of the classical pathway of complement activation by antibodies. Immunization with gp120 monomer or gp140 trimer antigens fused to proteins that form nanoparticles through self-assembly led to rapid concentration of these immunogens on LN FDCs as early as 24 h after injection<sup>36</sup>. Delivery of these particulate antigens to follicles was dependent on C3 and complement receptors. Complement activation was mediated by mannose-binding lectin (MBL), which bound with high avidity to the densely glycosylated HIV Env nanoparticles, but not the soluble forms of these immunogens. MBL binding enhanced GC responses, increased the production of long-lived plasma cells in bone marrow, and increased serum antibody responses<sup>36</sup>.

Both IC and nanoparticle immunization have been reported to enhance the immunogenicity of subunit vaccines in small and large animals, but the mechanisms underlying these enhancements remain poorly understood—especially in large animals, such as rhesus macaques that are similar to humans. Notably, these two approaches enhance complement binding to the immunogen, which may alter antigen fate in LNs. Here, we investigated the impact of IC formation and nanoparticle presentation on HIV Env immunogen trafficking in lymphoid tissues of nonhuman primates (NHPs). First, to enhance the formation of ICs, we passively administered, prior to immunization, a high-affinity macaque-derived monoclonal antibody (mAb)

that targets the base of the soluble HIV Env trimer immunogen BG505 SOSIP. In a second strategy, to enhance MBL binding and subsequent complement deposition, we multimerized the BG505 SOSIP HIV Env trimer immunogen in a particulate form: we recently described the development and characterization of several different two-component self-assembling nanoparticles that present viral glycoprotein immunogens<sup>37,38</sup>. Here, we assessed the in vivo trafficking properties of one such nanoparticle, T33-dn2, presenting the BG505 SOSIP trimer and compared it to soluble Env trimer immunogen. We applied these two immunization strategies in rhesus macaques, evaluating their impact on immunogen accumulation in draining LNs and localization within LN tissues. We found that both approaches promote the concentration of Env immunogens in B cell areas, with antigen accumulation in hundreds of follicles within a single LN. Nanoparticle immunogens were further shown to persist in follicles for at least a week, with a distribution suggesting accumulation on FDCs making up the light zone of nascent GCs. Thus, IC and nanoparticle (NP) immunizations can dramatically alter the localization of antigen in LNs, providing a rationale for their application in vaccine design platforms to promote humoral immunity against HIV and other infectious diseases.

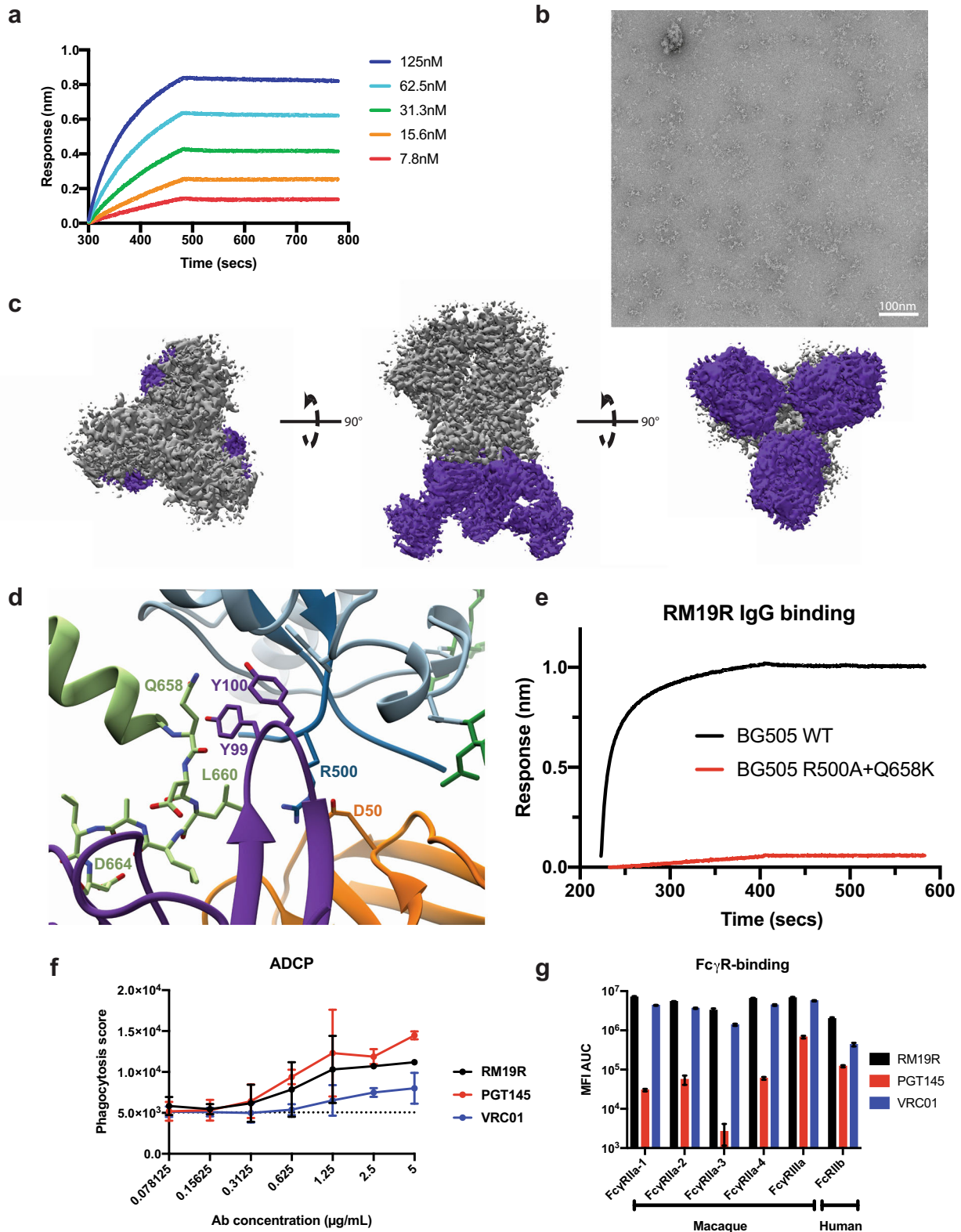
## RESULTS

Characterization of a rhesus macaque mAb, which recognizes the base of BG505 SOSIP Env trimers

The mAb RM19R was isolated from a BG505 SOSIP trimer-immunized rhesus macaque and was shown to bind to the base of the trimer by single particle negative stain-electron microscopy (NS-EM)<sup>39</sup>. Antigen-binding fragments (FABs) of RM19R bind to the BG505 SOSIP trimer with an affinity of 0.55 nM, as determined by biolayer interferometry (BLI) (Fig. 1a). RM19R IgG also forms ICs with the BG505 SOSIP in vitro as shown in Fig. 1b. To determine the molecular details of the RM19R epitope, we solved a 3.7 Å resolution cryo-EM structure of BG505 SOSIP in complex with RM19R FABs (Fig. 1c and Supplementary Fig. 1a–d). RM19R recognizes a quaternary epitope spanning two gp41 protomers and a single gp120 protomer that has 1316 Å<sup>2</sup> of buried surface area at the interface (Fig. 1c, d). RM19R uses two tyrosine residues at the tip of its CDR H3 to wedge between the C-terminal region of gp120 and the C terminus of gp41 in the adjacent protomer (Fig. 1d). Binding of RM19R causes the last seven residues (Q658 to D664) of the gp41 HR2 helix to unwind (Fig. 1d), but despite this conformational change, the complex is highly stable at room temperature for more than 24 h (Supplementary Fig. 1e). The light chain of RM19R also makes contact with the C5 region of gp120, and an arginine residue at position 500 in gp120 inserts between the heavy and light chains of RM19R (Fig. 1d). Consistent with the observations in the cryo-EM structure, binding of RM19R is eliminated by combining the mutations R500A and Q658K (Fig. 1e). RM19R complexed with BG505 SOSIP trimer activated antibody-dependent cellular phagocytosis (ADCP) at levels comparable with human bnAbs VRC01 and PGT145 (Fig. 1f). The Fc $\gamma$  receptor (Fc $\gamma$ R) binding profile after complexation with BG505 SOSIP showed strong binding to all macaque Fc $\gamma$ RIIa variants and macaque Fc $\gamma$ RIIIa-1 (Fig. 1g), comparable to VRC01 and much stronger than PGT145. These data suggest that RM19R would be capable of interacting with multiple Fc receptors in vivo.

IC formation redirects soluble Env immunogens to B cell follicles in LNs of mice and NHPs

To determine the impact of IC formation between BG505 SOSIP trimers and the base-directed RM19R antibody in vivo, we first analyzed trafficking of labeled RM19R and trimer by whole-tissue fluorescence imaging in mice. Groups of animals were passively immunized intravenously (i.v.) with doses of RM19R antibody



ranging from ~0.25 to 10 mg/kg, or phosphate-buffered saline (PBS) as a control. Twenty-four hours later, the animals were subcutaneously (s.c.) administered fluorescently labeled BG505 SOSIP trimer. At 24, 72, or 168 h following immunization, the animals were sacrificed and draining inguinal LNs were removed and fixed for imaging. Whole-tissue fluorescence imaging using a

Typhoon flatbed fluorescence scanner showed peak trimer accumulation in draining LNs at 1 day after immunization (Fig. 2a). In a separate experiment at the 24 h postimmunization time point only, confocal microscopy imaging of whole LNs after tissue clearing and staining for FDCs using an anti-CD35 antibody revealed substantial differences in the localization of the trimer

**Fig. 1 RM19R mAb binds to the base of Env trimer.** **a** BLI curves for immobilized RM19R FAB binding to BG505 SOSIP.v5.2 trimer as a function of SOSIP concentration. **b** Negative stain-EM image of BG505 SOSIP.v5.2 trimer/RM19R IgG in vitro immune complexes. Scale bar represents 100 nm. **c** Cryo-EM 3D reconstruction (3.7 Å resolution) of the BG505 SOSIP.v5.2.N241.N289 trimer/RM19R FAB complex. BG505 trimer density in gray with the RM19R FABs density in purple. **d** Binding pocket of RM19R CDR H3 with BG505, showing interactions between R500 and Q658 of BG505 with Y99 and Y100 of RM19R heavy chain (purple), RM19R light chain (orange), gp120 (blue), gp41 (light blue), glycans (green), and the adjacent gp41 (light green). **e** BLI curves of immobilized RM19R IgG to BG505.v5.2 (BG505 WT, black) or BG505 SOSIP.v5.2.N241.N289.R500A.Q658K (BG505 R500A+Q658K, red). Binding to RM19R is abolished by the combined mutations R500A and Q658K. **f** Antibody-dependent cellular phagocytosis (ADCP) assay comparing the propensity for RM19R, human VRC01, and human PGT145 antibodies to stimulate THP-1 cell phagocytosis when complexed with BG505 SOSIP on fluorescent beads. **g** Fc-γ receptor (FcγR) binding assay comparing RM19R, VRC01, and PGT145 binding to macaque FcγRIIIa and FcγRIIIb receptors or human FcγRIIIb receptor. MFI data were collected over a series of two-fold dilutions as in **f**, and the area under the curve is plotted for each combination. Error bars indicate SEM for duplicates.

immunogen in the presence of RM19R. BG505 trimer colocalized with B cell follicles in the presence of the RM19R in a dose-dependent manner (Fig. 2b, note that the relative positions and number of follicles revealed by the CD35 stain in each sample result from slightly different orientations of individual LNs in the images). This observation suggested that higher concentrations of antigen-specific antibodies resulted in more complete incorporation of the soluble antigen into ICs, which accumulated on FDCs.

We next carried out analogous experiments in rhesus macaques to compare antigen trafficking in large animals to our observations in mice. For this study, we labeled both the RM19R mAb and the BG505 SOSIP trimer, to enable tracking of both antigen and antibody. Pairs of NHPs were injected i.v. with fluorescently labeled RM19R mAb at 2.0 or 0.2 mg/kg, and 24 h later, all animals received s.c. injections of 50 µg BG505 SOSIP immunogen in each thigh; a control group was immunized s.c. with the trimer in the absence of RM19R passive transfer. Three days after antigen injection, animals were sacrificed and inguinal, iliac, axillary, popliteal, and mesenteric LNs were collected for analysis. Total RM19R and trimer accumulation in LNs were first measured by IVIS (in vivo imaging system) fluorescence imaging of excised tissues. To account for variability between animals in the number of LNs at a given site, we summed fluorescence signals for LNs collected at a common drainage location (e.g., all iliac LNs, or all axillary LNs). As expected from prior studies of antigen trafficking from this injection site in NHPs<sup>3</sup>, inguinal and iliac LNs were the primary draining LNs where SOSIP trimer accumulated (Fig. 3a). In line with the observations in mice, the total amount of trimer immunogen accumulating in these LNs was unaffected by the presence of passively transferred RM19R (Fig. 3a). In contrast, RM19R antibody showed preferential accumulation only in antigen-draining LNs, in an antibody dose-dependent manner (Fig. 3b).

We selected proximal draining LNs with total antigen signals representative of the median detected at each site for further analysis. Fluorescence imaging of fixed whole LNs at low magnification using a Typhoon flatbed fluorescence scanner showed an inhomogeneous distribution of trimer and RM19R mAb within the tissues (Fig. 3c). Antigen-draining LNs from animals receiving RM19R prior to trimer injection showed focal accumulations of the mAb across the tissue that we hypothesized represented B cell follicles; this focal accumulation appeared to be more intense in animals receiving the high dose of mAb. Inhomogeneity in the distribution was also detectable for the BG505 SOSIP trimer antigen in some LNs from animals that received the 2 mg/kg dose of the RM19R antibody (Fig. 3c, 2 mg/kg animal A inguinal LN). To obtain further insight into the distribution of antigen within the tissues, iliac LNs from each group were processed for whole-organ tissue clearing<sup>40,41</sup> and then imaged by light sheet microscopy. As shown in Fig. 3d and Supplementary Video 1, imaging of the cleared organs revealed strong colocalization of trimer and RM19R for animals receiving 2 mg/kg of the antibody, in as many as 500 follicles within a single LN. In accordance with the scanner images, the low-dose group exhibited RM19R antibody accumulation in follicles, but colocalization of the trimer signal was less pronounced. No fluorescent

signal above background was observed in the cleared samples from animals that did not receive passive transfer of the RM19R antibody. For both the IC and NP studies, the LN tissues were fixed prior to clearing or sectioning for histology. The loss of signal during tissue clearing indicates a substantial proportion of antigen is in a soluble compartment where crosslinking to nearby proteins/matrix does not occur—hence we suspect the majority of this material is in the sinuses and not the LN parenchyma. However, we cannot rule out the possibility that unfixed soluble antigen dispersed through the LN is removed by the clearing process, revealing only trapped ICs.

To investigate whether the apparent focal accumulation of ICs was, in fact, due to deposition on the FDC network of individual B cell follicles, we employed immunofluorescent staining of 100 µm tissue sections. Confocal microscopy of stained sections of the LNs revealed bands of antigen and RM19R antibody signal around the perimeters of CD35<sup>+</sup> FDC networks in multiple locations throughout each LN, corresponding to multiple B cell follicles (Fig. 3e). These ring-like accumulations of mAb and trimer correspond to the cross-sectional views through the cup-like, fluorescent three-dimensional (3D) structures observed in the light sheet imaging of whole tissues (Supplementary Video 2). Follicle accumulation of mAb/trimer was most apparent in animals that received the highest dose of RM19R, but was consistently observed in the low-dose samples as well. These tissue samples were not subjected to clarification treatment prior to imaging, and antigen fluorescence was still detected in the samples from animals immunized with trimer in the absence of RM19R mAb. However, the pattern of antigen distribution was much more diffuse, and not concentrated on the FDC network (Fig. 3e). Thus, immunization with BG505 SOSIP trimer antigens in the presence of the trimer base-specific antibody RM19R greatly increased antigen accumulation in follicles.

#### Production and characterization of a modular Env trimer protein nanoparticle

We next sought to compare the LN localization of ICs with a second strategy for promoting follicular localization, formulating Env trimers as protein nanoparticles<sup>36</sup>. Two-component, self-assembling nanoparticles represent a promising platform for presentation of HIV Env immunogens<sup>37,38,42,43</sup>. In this platform, the full-length ectodomain of Env (gp140) is genetically fused to the trimeric component of the nanoparticle and the fusion (antigen-bearing component) can be expressed and purified independently using an equivalent set of approaches applied with free soluble ectodomains. The antigen-bearing component is then combined with the corresponding second building block (assembly component) to form a nanoparticle of well-defined geometry (Fig. 4a). This system offers more flexibility and control compared to alternative approaches based on natural protein scaffolds (e.g., ferritin, E2p, lumazine synthase) or nanoparticles prepared from synthetic polymers or inorganic materials.

We employed a tetrahedral nanoparticle, T33\_dn2<sup>37,38</sup>, which consists of two trimeric building blocks (four copies of each), and

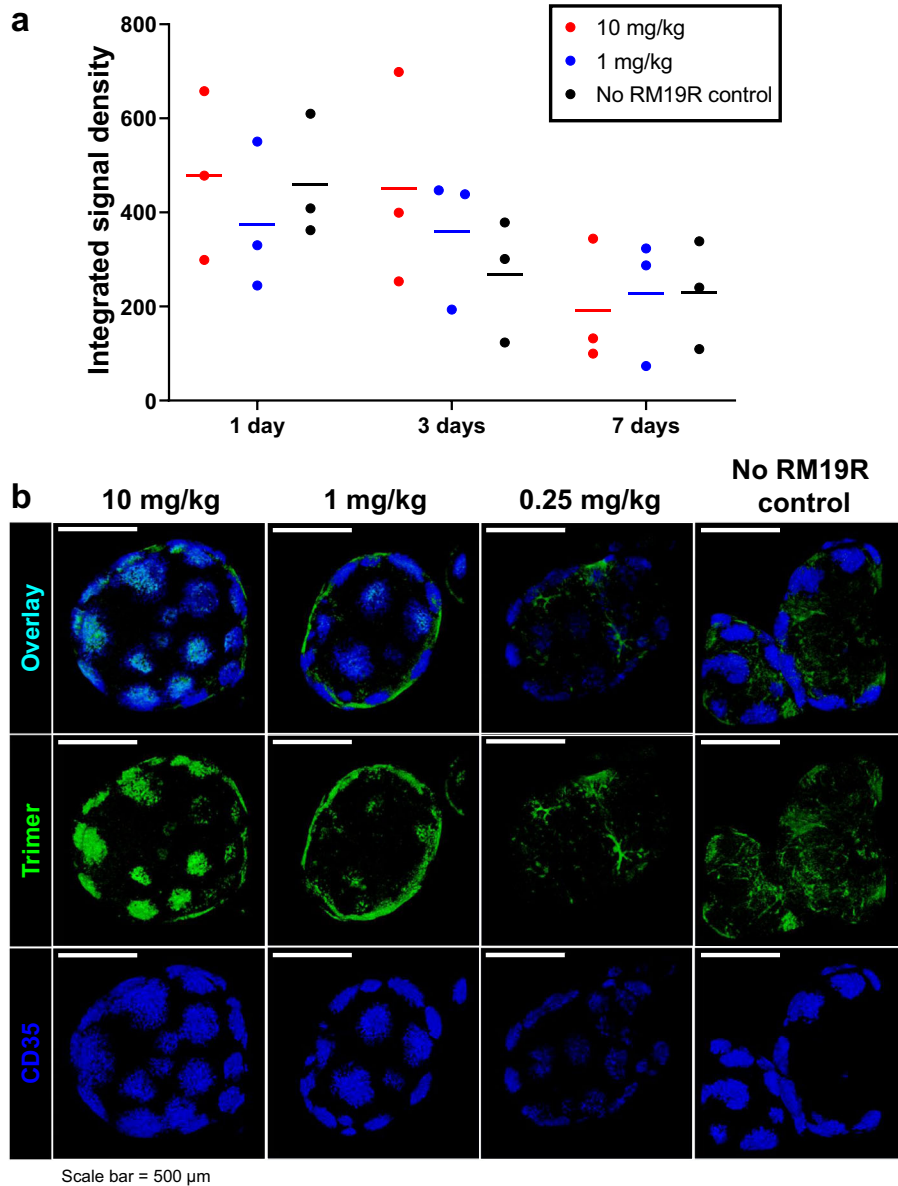


**Fig. 2 Immunization of mice with Env trimer in the presence of passively transferred antibody leads to rapid antigen accumulation in follicles.** Balb/c mice ( $n = 3/\text{group}$ ) were injected i.v. with different doses of RM19R mAb, followed 24 h later by s.c. immunization with 5  $\mu$ g Alexa Fluor 568-labeled BG505 trimer. Draining inguinal LNs were collected at various times after immunization for whole-tissue imaging. **a** Total trimer fluorescent signal in pairs of whole fixed inguinal LNs at 1–7 days postimmunization, as measured by flatbed fluorescence scanner. Data points are from individual animals, bars indicate mean of measurements from three animals. **b** 3D projections of whole cleared inguinal LNs 24 h after immunization, imaged by confocal microscopy to a depth of 300  $\mu$ m. Scale bars represent 500  $\mu$ m.

can present four SOSIP trimers. A variant of BG505 SOSIP, engineered to have increased soluble expression (see “Methods” for details), was fused to component A of the nanoparticle (T33\_dn2A). For particle production, BG505 SOSIP-T33\_dn2A was combined with equimolar amounts of the assembly component (T33\_dn2B) and incubated for 24 h, leading to >90% assembly efficiency (Supplementary Fig. 2a). Sodium dodecyl sulfate-polyacrylamide gel electrophoresis (SDS-PAGE) analysis confirmed the presence of both BG505 SOSIP-T33\_dn2A and T33\_dn2B components in the purified nanoparticle sample (Supplementary Fig. 2a). NS-EM analysis revealed that the purified nanoparticles were highly homogeneous (Supplementary Fig. 2b). BG505 SOSIP-T33\_dn2 nanoparticles were then subjected to cryo-EM for structural analysis (Fig. 4, Supplementary Fig. 3, and Supplementary Table 1). An initial cryo-EM reconstruction of the entire

nanoparticle verified the appropriate assembly to the target tetrahedral architecture with four BG505 SOSIP trimers flexibly linked to the nanoparticle core (Fig. 4a). The particle diameter is ~37 nm and the average apex–apex distance between the BG505 SOSIP trimers is 31 nm. Due to the flexible nature of the linker connecting the BG505 SOSIP antigen and T33\_dn2A scaffold, high-resolution reconstruction of the entire nanoparticle as a single model could not be performed. However, focused refinement in combination with partial signal subtraction allowed us to treat the nanoparticle core (consisting of T33\_dn2A and T33\_dn2B) and the displayed BG505 SOSIP trimers as separate subparticles and analyze them independently. Using the approach described in the “Methods” section and Supplementary Fig. 3a, we reconstructed a 4.6 Å resolution map of the nanoparticle core (Fig. 4b) and a 4.5 Å resolution map of the BG505 SOSIP trimer

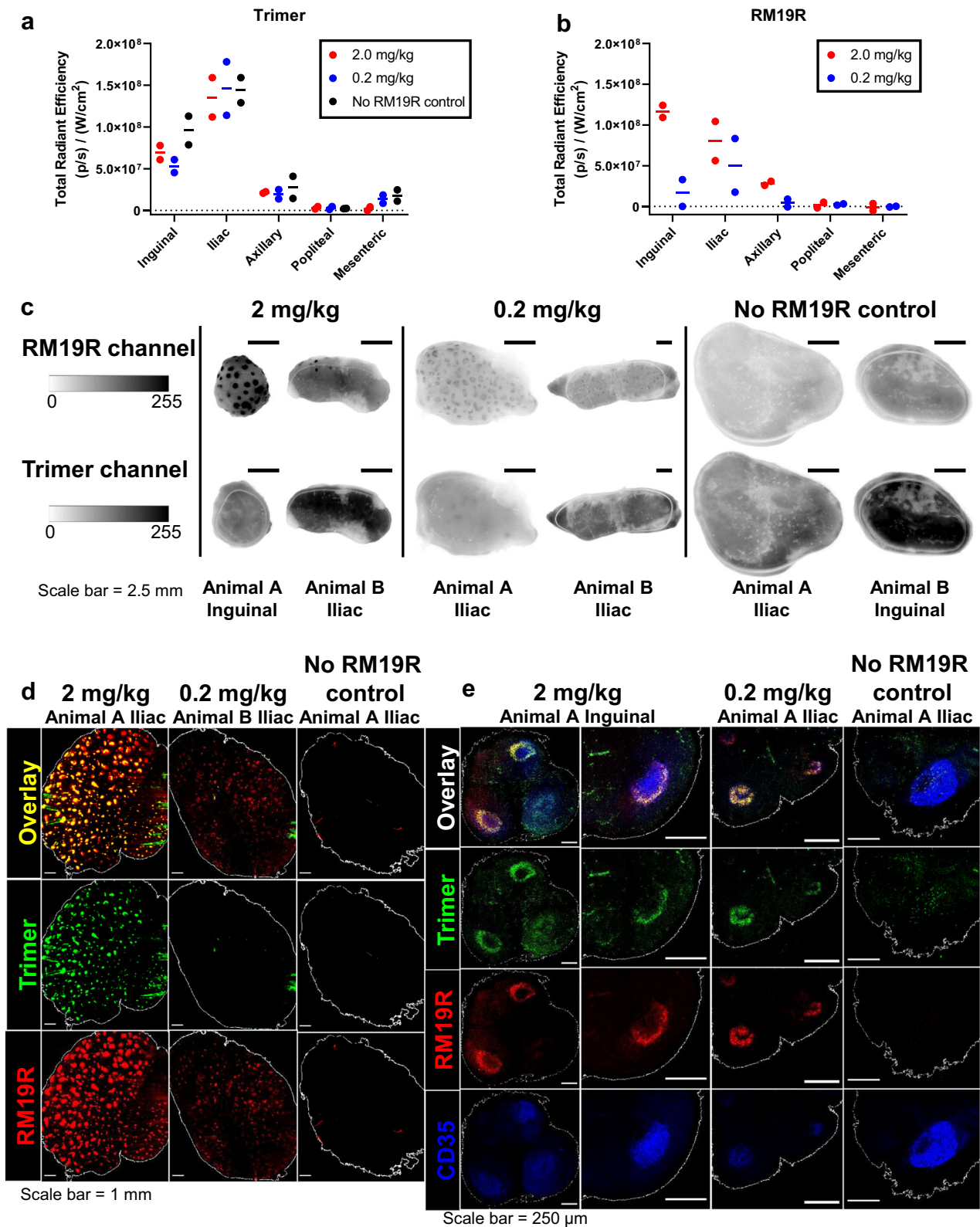


(Fig. 4c, Supplementary Fig. 3a). A combination of Rosetta relaxed refinement and manual refinement in Coot was applied to generate the atomic models (Supplementary Table II, Fig. 4b, c). The refined model of the T33\_dn2 nanoparticle core revealed a high degree of correlation with the design model predicted by Rosetta at the backbone level. When compared to Rosetta models,

Ca root-mean-square deviation values for the trimeric T33\_dn2A and T33\_dn2B components were 1.20 and 0.81 Å, respectively (Supplementary Fig. 3b). The C-terminal helix in T33\_dn2B was not resolved in the EM map, suggesting a high degree of flexibility, which may be at least partially influenced by the 6xHis-tag immediately following this sequence. Importantly, the structure of

**Fig. 3 Immunization of NHPs with Env trimer in the presence of passively transferred antibody leads to rapid antigen accumulation in follicles.** Rhesus macaques ( $n = 2/\text{group}$ ) were injected i.v. with different passively doses of Alexa Fluor 647-labeled RM19R mAb, followed 24 h later by s.c. immunization with 50  $\mu\text{g}$  Alexa Fluor 568-labeled BG505 trimer in each mid thigh. LNs from indicated locations were harvested 3 days after immunization. Data points are from individual animals; bars indicate mean of measurements from two animals. **a** Total fluorescent signal corresponding to trimer from all LNs from each animal at a particular site, as measured by IVIS. **b** Total fluorescent signal corresponding to RM19R antibody from all LNs from each animal at a particular site, as measured by IVIS. **c** Selected images of whole uncleared LNs from fluorescent flatbed scanner imaging in each channel. Scale bars represent 2.5 mm. **d** Maximum projections of whole cleared LNs from draining LN locations for each group, as imaged by light sheet microscopy. Scale bars represent 1 mm. **e** Single planes of uncleared 100- $\mu\text{m}$ -thick LN sections immunofluorescently stained for FDCs, as imaged by confocal microscopy. Scale bars represent 250  $\mu\text{m}$ .

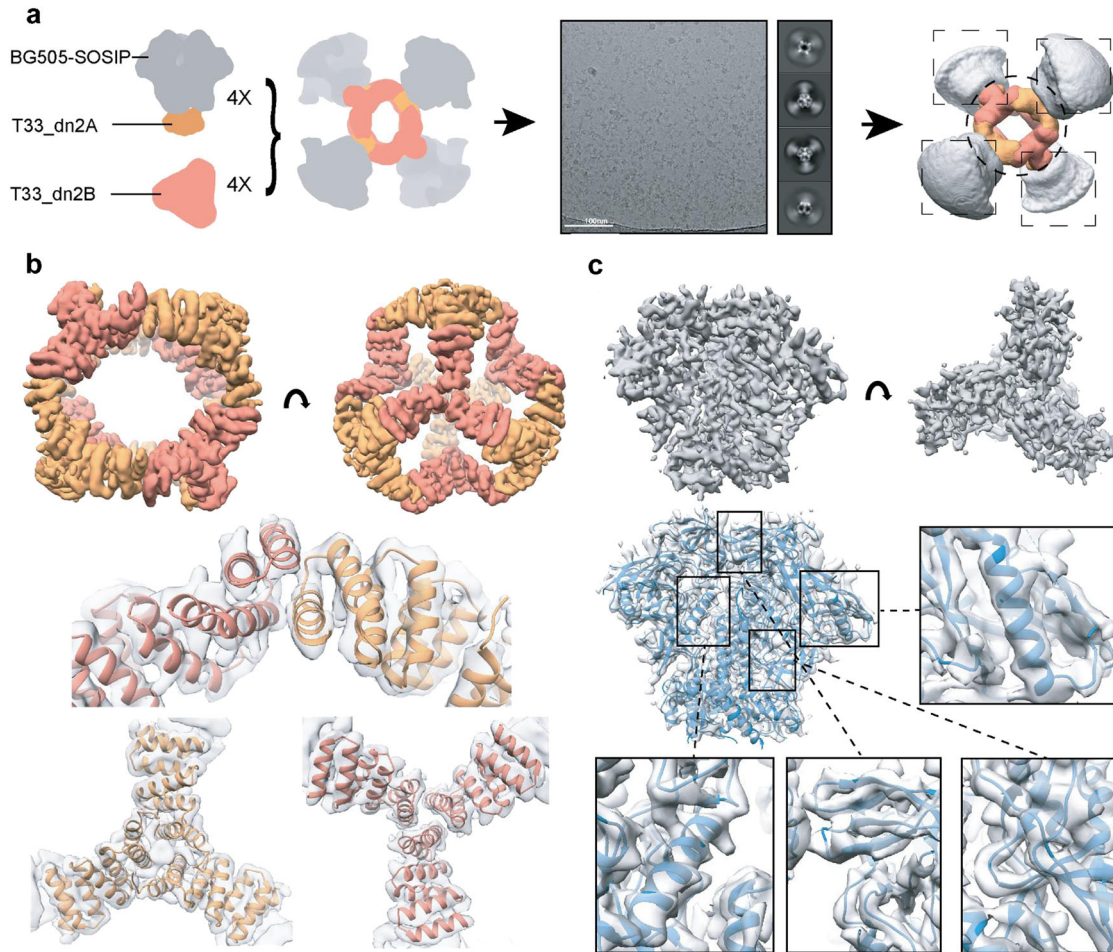


**Fig. 4 BG505 SOSIP-T33\_dn2 nanoparticle self assembles in a tetrahedral arrangement.** **a** Cryo-EM analysis of the BG505 SOSIP-presenting T33\_dn2 nanoparticle. Dashed boxes around the model structure at right indicate the segmented data processing approach where the trimer and nanoparticle components were analyzed separately in the TEM data. **b** Post-processed cryo-EM map of the nanoparticle core and the fit of refined model to the reconstructed density (T33-DN2-A and T33-DN2-B components are colored in orange and salmon, respectively). **c** Post-processed cryo-EM map of the nanoparticle-presented BG505 SOSIP trimer following subparticle analysis and model to map fit of the refined model.

the scaffolded BG505 SOSIP revealed that the antigen remains in the native-like, pre-fusion state and that nanoparticle incorporation did not interfere with its structure. Extensive antigenicity analysis of the BG505 SOSIP-T33\_dn2 nanoparticle reported elsewhere<sup>37,38</sup> also supports this conclusion.

#### MBL recognizes BG505 Env trimer nanoparticles

We previously showed that Env trimers displayed on a ferritin nanoparticle core could be recognized by the innate immunity protein MBL, via the dense glycan coat on the trimer surfaces<sup>36</sup>. We therefore evaluated the capacity of free trimeric BG505 SOSIP or BG505 SOSIP presented on tetrahedral T33\_dn2 nanoparticles

to interact with MBL *in vitro*. Recombinant human MBL-2 was incubated with BG505 SOSIP or BG505 SOSIP-T33\_dn2 in buffer containing 2 mM  $\text{CaCl}_2$  and imaged using NS-EM as described in the “Methods” section. NS-EM analysis confirmed the presence of high molecular weight species in both samples (Supplementary Fig. 4a). However, EM data interpretation is complicated by the fact that MBL-2 itself exists in different oligomeric forms, some of which are  $\sim 20$  Å in diameter or larger (Supplementary Fig. 4a). MBL-2 and antigen complex solutions were therefore also analyzed by size-exclusion chromatography (SEC) (Supplementary Fig. 4b, c). Env trimer alone eluted primarily as a single peak in SEC (Supplementary Fig. 4b). When mixed with MBL-2, a small peak at low elution volume was detected, indicative of a limited formation

of MBL/trimer aggregates. Surprisingly, MBL-2 also appeared to induce partial trimer disassembly and an increase in monomer/dimer species (Supplementary Fig. 4b). By contrast, BG505 SOSIP-T33\_dn2 nanoparticles appeared to co-assemble into a greater proportion of higher molecular weight species when incubated with MBL-2 (Supplementary Fig. 4c). The aggregate fractions were subjected to NS-EM and SDS-PAGE analysis (Supplementary Fig. 4d, e). NS-EM analysis revealed the existence of large complexes of different sizes with discernable nanoparticles that appear to be clustered. SDS-PAGE confirmed the presence of both nanoparticle and MBL-2 in the aggregate sample. These biophysical measurements suggest that despite the modest antigen valency of the BG505 SOSIP-T33\_dn2 nanoparticle, it can readily interact and co-aggregate with MBL that will be present in interstitial fluid.

Nanoparticle trimer immunogens accumulate in follicles of NHPs following immunization

We next designed an experiment to compare antigen trafficking of soluble BG505 SOSIP MD39 trimer<sup>9</sup> and BG505 SOSIP-T33\_dn2 nanoparticle immunogen in rhesus macaques. The immunogen dose was normalized based on the total amount of BG505 SOSIP (100 and 142 µg per dose per animal for free trimer and nanoparticle, respectively). Each animal received half of the total dose of AF647-labeled immunogen mixed with an immune stimulating complex (ISCOM)-like saponin adjuvant s.c. in each of their left and right inner thighs. Groups of three animals were sacrificed either 2 or 7 days postimmunization, and LNs from primary draining sites (inguinal and iliac), as well as distal sites (axillary), were harvested for imaging analysis.

We first analyzed the total antigen content of fixed LNs using the Typhoon scanner, summing the total antigen fluorescence signal of all LNs at each collection site as performed in the IC experiments. These measurements revealed a 37% lower accumulation of the antigen in the proximal iliac draining LNs for animals immunized with the nanoparticle compared to the soluble trimer immunogen at 2 days postimmunization (Fig. 5a). Representative Typhoon images of draining iliac LNs from each group at days 2 and 7 are shown in Fig. 5b. Both trimer and NP-immunized groups showed diffuse antigen signal across the tissues in the whole unmanipulated tissue imaging at day 2. At day 7, the signal dropped in both groups, but the remaining signal in the NP-immunized LNs was strikingly distributed in a follicular pattern as observed in our IC immunizations (Fig. 5b). We next selected individual antigen-positive LNs from each group (or naive LN controls) and cleared them for light sheet imaging. Similar to results from the IC experiment, we observed little to no fluorescence above background in cleared organs from animals receiving soluble BG505 SOSIP trimer and adjuvant at either 2 or 7 days postimmunization (Fig. 5c and Supplementary Video 3). In striking contrast, all LNs from animals that received BG505 SOSIP presented on the T33\_dn2 nanoparticle displayed bright and obvious focal accumulations of the immunogen throughout the LNs, with up to 500 such follicular deposits observed in a single LN (Fig. 5c and Supplementary Video 3). Similar to the cleared tissue images from the IC studies, it is unclear if the signal observed in Typhoon scanning that is lost in the cleared tissue images for the soluble trimer represents antigen that has penetrated the LN or is accumulated in the sinuses, and thus the low signal in this group may represent an artifact of extracting unfixed antigen. However, the concordance of Typhoon and light sheet imaging for the day 7 nanoparticle samples suggests that, at this later time, the majority of NP antigen has localized in follicles.

Next, histological sections of the main draining LNs were stained with anti-CD35 to identify the FDC networks, to confirm that the focal accumulations observed in the LNs of immunized animals are in fact in B cell follicles. We observed the accumulation of nanoparticle immunogen, but not free trimer, in and around B

cell follicles (Fig. 5d). Free trimer was instead detected at low levels in the interior medullary regions of LNs, which may indicate uptake by DC-SIGN<sup>+</sup> macrophages, as suggested by Park et al.<sup>20</sup>. By co-staining the histological sections of draining LNs with the proliferation marker Ki67, we detected GC induction in both trimer and nanoparticle-immunized animals at day 7 (Fig. 5d). However, free trimer was only detected in follicles very infrequently, suggesting very low levels of antigen in the GCs, while substantial levels of the nanoparticle-presented trimer were found in these sites. Thus, formation of protein nanoparticles with as few as four Env trimers was sufficient to significantly alter immunogen trafficking in NHPs and increase delivery to B cell follicles.

## DISCUSSION

Availability of antigen in GCs is critical for affinity maturation of the B cell response, but delivery of immunogens to follicles (and subsequent GCs) in a primary immunization is often inefficient for soluble antigens. This is particularly true for soluble HIV Env trimer immunogens, which have been reported in mice to localize to interfollicular macrophages<sup>20,36</sup>. Efficient immunogen delivery to follicles may be critical because antigens are rapidly degraded in vivo<sup>44</sup>; hence, the availability of neutralizing epitopes likely decays over time. Here, we tested two different approaches aiming to promote complement-mediated delivery of Env trimer immunogens to follicles: (1) in vivo formation of ICs with a passively transferred anti-Env mAb, and (2) generation of self-assembling protein nanoparticles displaying four copies of stabilized Env trimers. We found that both IC and nanoparticle immunization approaches led to a concentration of antigen ringing the periphery of B cell follicles in the draining LNs of NHPs. Light sheet imaging of whole cleared LNs revealed that both immunization strategies led to accumulation of the immunogens in follicles throughout the entire LN tissue, concentrating in as many as 500 follicles in a single draining LN. While both IC and NP immunization have been previously reported to enhance output measures of the humoral immune response to subunit vaccines, our data provide evidence in the closest animal model to humans that these immunization strategies alter immunogen trafficking in a manner that may help drive effective B cell responses.

Extensive progress has been made in the past 10 years in the engineering of stable soluble forms of the HIV Env protein that faithfully replicate the antigenic structure of the native viral Env for potential use in a subunit vaccine<sup>5-7,9,10,45</sup>. However, it has been shown that glycans of soluble Env trimers are recognized by SIGN-R1-expressing macrophages in LNs, leading to the capture of Env immunogens in interfollicular regions of LNs following immunization<sup>20,36</sup>. Env immunogen accumulation on FDCs has been demonstrated by using novel immunization strategies that deliver antigen over time periods of several weeks through implanted osmotic pumps or repeated injections<sup>46,47</sup>, but such strategies may not be clinically practical.

IC vaccines have been studied for many years preclinically<sup>28</sup> and have also entered clinical trials<sup>31,32,48</sup>. In the setting of HIV vaccines, complexation with mAbs has been used to alter the accessibility of neutralizing vs. non-neutralizing epitopes or alter conformations of the immunogen, promoting B cell responses against neutralizing epitopes<sup>28</sup>. Motivated by the recent findings that the base of Env trimers is a highly immunodominant non-neutralizing target on SOSIP immunogens<sup>46,49,50</sup>, we utilized a mAb isolated from macaques recognizing a base epitope for IC formation, with the goal of masking humoral responses against the base. To allow for the in vivo formation of ICs, we preinjected animals i.v. (i.e., passively immunized) with the base-specific RM19R mAb 24 h prior to antigen administration. While many preclinical studies of IC immunization employ ICs formed ex vivo prior to injection to conserve antibody<sup>27,51</sup>, the passive mAb administration used here was selected to both test the impact of

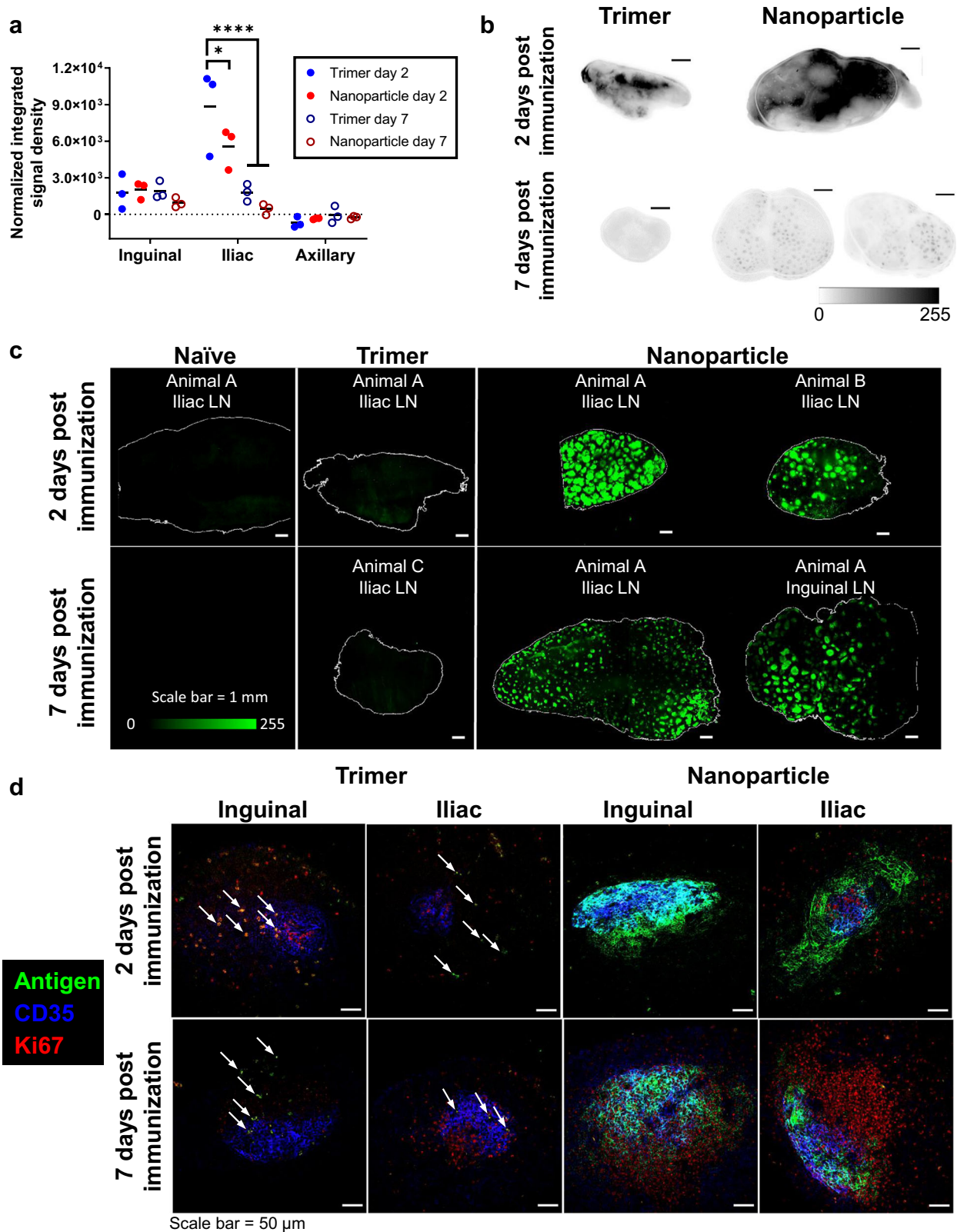


**Fig. 5 Immunization of NHPs with nanoparticle leads to rapid antigen accumulation in follicles without passively transferred antibody.** **a** Total fluorescent signal corresponding to trimer or nanoparticle immunogen, normalized by degree of labeling per trimer. Data points are the summation from all LNs from a particular site for each animal, as measured by fluorescent flatbed scanner. Bars indicate the mean of three animals. \* $P = 0.0245$ , \*\*\*\* $p \leq 0.0001$  by two-way ANOVA. **b** Representative images of whole uncleared LNs from fluorescent flatbed scanner imaging of labeled SOSIP immunogen. Scale bars represent 2.5 mm. **c** 3D projections of whole cleared LNs from draining LN locations for each group, as imaged by light sheet microscopy. Scale bars represent 1 mm. **d** Single planes of uncleared 100-µm-thick LN sections immunofluorescently stained for FDCs and Ki67, as imaged by confocal microscopy. Scale bars represent 50 µm.

monoclonal Ab IC formation on immunogen trafficking and model potential effects of boosting animals with pre-existing anti-trimer antibody. Furthermore, we believe this represents an important model for how IC formation affects subunit vaccines, especially for those in which patients likely have pre-existing immunity (e.g., influenza virus and respiratory syncytial virus).

NPs have been reported to exhibit a variety of different distribution patterns *in vivo*. As with ICs, innate immunity factors appear to play a significant role in directing the antigen to LN follicles. Link et al.<sup>52</sup> showed that Q $\beta$  antigens administered to naive animals only accumulated on the FDC network when they were in a virus-like particle (i.e., an NP) format, not as a soluble dimer. This process was mediated by nlgM and complement. We also recently identified a role for innate immune recognition of particulate HIV antigens in mice<sup>36</sup>. This pathway involves recognition of the highly glycosylated residues on Env-based immunogens via MBL. MBL binding resulted in a complement attachment, which directed the NPs to FDCs. Importantly, MBL only bound to NP forms of immunogens, and not soluble subunits, likely due to a requirement for multivalent engagement of MBL with the glycan patches of multiple trimers for stable binding. Due to the success of this approach in mice, we wanted to test if the same principles would hold true in NHPs. Furthermore, to help clarify the degree of antigenic valency that is required for promoting interactions with MBL and directing NP antigen to FDCs, we tested here a new protein NP scaffold that displays only four trimers. This was half the number from the ferritin scaffold used in the previous mouse study, but the diameters of the two Env-presenting nanoparticles were very similar (~35–40 nm). As a result, the spacing between the antigens is almost two times higher in the case of T33\_dn2 nanoparticle (~31 nm apex–apex distance) versus the ferritin nanoparticle (estimated apex–apex distance for two nearest neighboring trimers ~15–20 nm).

We found that both the IC approach and the NP approach were successful in delivering antigen to the FDC network of LN follicles. In both cases, this contrasted to the distribution of soluble Env trimer immunogen in LNs, despite similar or even lower total amounts of antigen accumulation within draining LNs. Concentration of antigen in follicles was observed by multiple methods, including by whole-organ clarification and by tissue sectioning and immunofluorescent staining. Notably, the patterns of antigen concentration around the periphery of follicles described here mirror histological findings recently published for NHPs immunized with antigen-displaying liposomes, and the data we recently reported demonstrating antigen deposition in the follicles of animals receiving sustained antigen delivery via osmotic pumps or repeated injections<sup>46,47,53</sup>. The similarity in antigen accumulation patterns in the latter study lends support to the hypothesis that ICs formed with early antigen-specific IgM and IgG were the driving factors for FDC deposition in those “slow delivery” vaccine administration studies.

Unexpectedly, we found that a statistically significant greater amount of soluble trimer had accumulated in draining LNs compared to the NP immunogen 2 days postimmunization. This contrasts with our findings in mice for trafficking of two other protein nanoparticle immunogens, where we saw that at 3 days postinjection, both a trimer-ferritin nanoparticle and gp120-lumazine synthase nanoparticle accumulated to higher peak levels in the LN than soluble antigen controls<sup>36</sup>. This may reflect different LN accumulation kinetics for soluble vs. NP trimer, whereby the peak of antigen accumulation may occur at a timepoint between 2 and 7 days, but we were unfortunately limited in the number of timepoints we could sample in this study.

We recently completed initial immunogenicity studies evaluating T33\_dn2 nanoparticles presenting a different HIV Env trimer based on a consensus sequence of group M genotypes, ConM SOSIP<sup>38</sup>. In rabbits, soluble ConM SOSIP and T33\_dn2 nanoparticles elicited equivalent trimer-specific antibody responses.

However, there was also a substantial antibody response to the underlying nanoparticle scaffold, suggesting that the total antibody response in this group was greater than the trimer-alone group. The nanoparticle response is inherently “off-target” and we are now working on ways to suppress this phenomenon. Despite these engineering challenges, a number of studies have shown enhanced Env-specific humoral responses elicited by particulate immunogens<sup>54–56</sup>, and our conclusion that follicular targeting ultimately enhances humoral responses is supported by studies of two other protein nanoparticles, eOD-GT8 60mer and BG505 SOSIP trimer-ferritin particles, where follicular localization in mice was associated with enhanced GC and antibody responses against the Env immunogens<sup>36</sup>.

Antibodies formed in response to slow delivery immunization regimes were found to exhibit enhanced tier 2 HIV virus neutralization and to bind to a more diverse set of epitopes on soluble trimers, which may have been due to the enhanced capture and preservation of the immunogen on FDCs<sup>46</sup>. We believe that by achieving similar degrees of capture and preservation with bolus administration, it may be possible to evoke similar high-quality antibody responses with ICs or NPs. Additional studies to test for such immune responses are underway.

## METHODS

### Env protein production

For IC trafficking studies, soluble BG505 SOSIP trimers were employed. The N241 and N289 N-linked glycosylation sites (mutations P240T, S241N, M271I, F288L, T290E, and P291S) were introduced into the BG505 SOSIP.v5.2 pPPI4 vector<sup>57</sup> using the QuikChange® Lightning Site-Directed Mutagenesis Kit (Agilent). The R500A and Q658K mutations were added to the BG505 SOSIP.v5.2.N241.N289 vector. Sequences were verified by Sanger sequencing (Genewiz). Three different closely related BG505 SOSIP.v5.2 trimers were used in the studies as indicated below: BG505 SOSIP.v5.2, BG505 SOSIP.v5.2.N241.N289, and BG505 SOSIP.v5.2.N241.N289.R500A. Q658K were expressed in HEK293F cells (Invitrogen) and purified with PGT145 affinity chromatography, followed by SEC using a HiLoad® 16/600 Superdex® pg200 (GE Healthcare) as described previously<sup>57</sup>.

For studies comparing soluble trimer with tetrameric trimer nanoparticles, we employed untagged BG505 SOSIP MD39 trimers<sup>9</sup>. The protein was expressed in FreeStyle 293F cells (Thermo Fisher Scientific; Cat# R79007) and purified by immunoaffinity purification using 2G12 mAb as previously described<sup>7</sup>. Briefly, clarified supernatants were passed over 2G12 mAb immobilized on CNBr-activated Sepharose 4B resin (GE Healthcare; Cat# 17043001). The resin was washed with Tris-buffered saline (TBS) and captured trimer was eluted with 3 M MgCl<sub>2</sub> and immediately buffer exchanged into fresh TBS. Proteins were concentrated and subjected to SEC on a HiLoad 26/600 Superdex 200 pg (GE Healthcare; Cat# 28989336). Trimer-containing fractions were pooled, concentrated to 1 mg/mL, and flash frozen on liquid nitrogen in 100  $\mu$ L aliquots and stored at  $-8^{\circ}\text{C}$  until further use. All steps were performed under low-endotoxin conditions and the final preparation was confirmed to be  $<2.5$  EU/mg using an Endosafe-PTS system (Charles River; Cat# PTS100).

### Antibody IgG and Fab production

The sequences encoding rhesus macaque IgG1 heavy chain of RM19R and the rhesus macaque kappa chain of RM19R were codon optimized, synthesized, and separately cloned into the pcDNA3.4 vector using the GeneArt service from Invitrogen. The RM19R IgG was produced by transient transfection of Expi293 cells and purified using Protein A affinity chromatography by Invitrogen. Human VRC01 and PGT145 were produced in HEK293F cells (Thermo Fisher) and purified using Protein A affinity resin (Thermo Fisher) as previously described<sup>58,59</sup>. The RM19R Fab heavy-chain plasmid was made introducing two stop codons following residue D234 in the RM19R IgG1 heavy-chain vector using the QuikChange® Lightning Site-Directed Mutagenesis Kit (Agilent). The RM19R FAB was expressed in HEK293F cells (Invitrogen) by co-transfecting with the FAB heavy and kappa chain plasmids (1:1 ratio) using PEImax. Transfection supernatant was harvested after 6 days and passed through a 0.45  $\mu$ m filter. The RM19R

Fab was purified using CaptureSelect™ CH1-XL (Thermo Fisher) affinity chromatography.

### BG505 SOSIP-T33\_dn2 nanoparticle component production

BG505 SOSIP engineered with stabilizing mutations from SOSIP.v5.2<sup>57</sup> (A501C, T605C, I559P, E64K, A73C, A316W, A561C) and MD39<sup>9</sup> (M271I, A319Y, R585H, L568D, V570H, R304V, F519S) and glycan knock-ins at positions N241 (mutations: P240T, S241N) and N289 (mutations: F288L, T290E, P291S) was fused to component A of the T33\_dn2 nanoparticle and subcloned into a pPPI4 vector as described previously<sup>38</sup>. The vector with antigen-bearing component was transfected into FreeStyle 293F cells using polyethylenimine (Polysciences Inc.) as described previously<sup>7</sup>. Six days post transfection, the cells were removed by centrifugation (10,000 × *g* for 1 h at 4 °C) and the supernatant was cleared by vacuum filtration (0.45 μm filtration units, Millipore Sigma). BG505 SOSIP-T33\_dn2A component was purified from the cleared supernatant using Sepharose 4B resin (GE Healthcare Life Sciences) carrying PGT145 IgG. The resin was washed with buffer containing 25 mM Tris-HCl + 500 mM NaCl (pH 7.4) and the protein was eluted using buffer containing 3 M MgCl<sub>2</sub> + 250 mM L-arginine (pH 7.2). The eluate was collected into an equal volume of the SEC buffer (25 mM Tris + 500 mM NaCl + 250 mM L-arginine + 5% glycerol, pH 7.4). The sample was concentrated and buffer exchanged to the SEC buffer using Amicon ultrafiltration units with 100 kDa cutoff (Millipore Sigma). A HiLoad 16/600 Superdex S200 pg column was used for the gel filtration step. The protein was concentrated and stored in SEC buffer at 4 °C until nanoparticle assembly. The T33\_dn2B component of the nanoparticle was expressed in *Escherichia coli*. BL21-DE3 cells (NEB) were transformed with pET28b vector carrying T33\_dn2B gene with a C-terminal His-tag. Following inoculation, the cells were incubated in self-inducible media<sup>37</sup> and shaken at 16 °C for ~18 h. BL21 cells were spun down (5000 × *g*, 30 min, 4 °C) and resuspended in TBS (Alfa Aesar) containing cComplete™ protease inhibitor cocktail (Sigma Millipore). The cells were lysed using sonication and pressurized disruption. Cell lysate was cleared by centrifugation at 10,000 × *g* for 1 h at 4 °C, filtered (0.45 μm filtration units, Millipore Sigma) and loaded onto a cComplete™ His-Tag Purification Resin gravity column (Sigma Millipore). The resin was first washed with detergent-containing buffer (25 mM Tris + 500 mM NaCl + 0.5% *N*-dodecyl-β-D-maltoside, pH 7.2) and then with low imidazole buffer (25 mM Tris + 500 mM NaCl + 20 mM imidazole, pH 7.2). Detergent buffer wash helped remove endotoxin from the sample. The sample was eluted using high imidazole buffer (25 mM Tris + 500 mM NaCl + 500 mM imidazole, pH 7.2), concentrated and buffer exchanged to the same SEC buffer as described above using Amicon ultrafiltration units with 10 kDa cutoff (Millipore Sigma). Finally, T33\_dn2B was SEC purified using HiLoad 16/600 Superdex S200 pg column.

### Nanoparticle assembly, purification, and labeling

Nanoparticle components (BG505 SOSIP-T33\_dn2A and T33\_dn2B) were concentrated to ~1 mg/mL and equimolar amounts were combined and incubated for 24 h at 4 °C, for nanoparticle assembly. Assembled nanoparticles were purified from the unassembled components using Sephacryl S-500 HR column using Dulbecco's phosphate-buffered saline (Thermo Fisher Scientific) as the running buffer. ToxinSensor™ Single Test Kit (GenScript) was applied to verify that the endotoxin levels of the labeled nanoparticle were below 50 EU/kg per dose.

### Fluorescent labeling

RM19R IgG was labeled with the Alexa Fluor™ 647 Protein Labeling Kit (Thermo Fisher) to a degree of labeling (DoL) of 7.1 fluorophores per Ab. The BG505 SOSIP.v5.2.N241.N289 trimer was labeled with the Alexa Fluor™ 568 Protein Labeling Kit (Thermo Fisher) to a DoL of 8.3 fluorophores per trimer. The MD39 SOSIP trimer was labeled with the Alexa Fluor™ 647 Protein Labeling Kit (Thermo Fisher) to a DoL of 4.1 fluorophores per trimer. For the BG505 SOSIP-T33\_dn2 nanoparticle, 2 mg of concentrated nanoparticles were labeled using an Alexa Fluor™ 647 Protein Labeling Kit (Thermo Fisher). The final DoL was 42.1 fluorophores per nanoparticle; 10.5 per trimer.

### Biolayer interferometry (BLI)

An Octet RED instrument (ForteBio) was used to determine the kinetic parameters of the RM19R/BG505 SOSIP interaction by BLI. The RM19R Fab was loaded onto anti-human Fab-CH1 (FAB2G) biosensors (ForteBio) at a

concentration of 10 μg/mL in kinetics buffer (PBS, pH 7.4, 0.01% (w/v) bovine serum albumin (BSA), and 0.002% (v/v) Tween-20) until response of 1 nm shift was reached. The loaded biosensors were dipped into kinetics buffer for 1 min to acquire a baseline and then moved to wells containing a series of 2-fold dilutions of BG505 SOSIP.v5.2 in kinetics buffer, starting at a 125 nM. The trimers were allowed to associate for 180 s before the biosensors were moved back to the wells containing kinetics buffer where the baseline was acquired. Dissociation of the trimers from the Fab-loaded biosensors was recorded for 300 s. Kinetic parameters were calculated using the Octet System Data Analysis v9.0 (ForteBio). To assess how the R500A and Q658K mutations impact binding of RM19R, the IgG was loaded onto anti-human IgG Fc capture (AHC) biosensors (ForteBio) at a concentration of 5 μg/mL in kinetics buffer until response of 1 nm shift was reached. The loaded biosensors were dipped into kinetics buffer for 1 min to acquire a baseline and then moved to wells containing either BG505 SOSIP.v5.2 or BG505 SOSIP.v5.2.N241.N289.R500A.Q658K, both at a concentration of 1000 nM in kinetics buffer. The trimers were allowed to associate for 180 s before the biosensors were moved back to the wells containing kinetics buffer where the baseline was acquired. Dissociation of the trimers from the IgG-loaded biosensors was recorded for 180 s.

### Negative stain-electron microscopy

NS-EM experiments were performed as described previously<sup>60,61</sup>. Fusion components and assembled nanoparticle samples were diluted to 20–50 μg/mL and loaded onto the carbon-coated 400-mesh Cu grid that had previously been glow discharged at 15 mA for 25 s. Grids were negatively stained with 2% (w/v) uranyl-formate for 60 s. Data collection were performed on either an FEI Tecnai T12 microscope (2.05 Å/pixel; ×52,000 magnification) or FEI Talos microscope (1.98 Å/pixel; ×72,000 magnification). The electron dose was set to 25 e<sup>-</sup>/Å<sup>2</sup> and images were collected with a defocus value of -1.50 or -2.00 μm. The micrographs were recorded on a Tietz 4k × 4k TemCam-F416 CMOS or a FEI Ceta 16M camera using a Leginn automated imaging interface<sup>62</sup>. Data processing were performed in Appion data processing suite. With nanoparticle samples, ~500–1000 particles were manually picked from the micrographs and 2D classified using the Iterative MSA/MRA algorithm. With trimer samples, 10,000–40,000 particles were auto-picked and 2D classified using the Iterative MSA/MRA algorithm. For 3D classification and refinement, we continued processing in Relion/3.0b3<sup>63</sup>.

### BG505 SOSIP/RM19R Fab complex

Seven hundred micrograms of the BG505 SOSIP.v5.2.N241.N289 trimer was mixed with ~1.4 mg RM19R Fab and incubated at RT overnight. The complex was SEC purified using a Superose™ 6 Increase 10/300 GL (GE Healthcare) column in TBS. Fractions containing the complex were concentrated to 13 mg/mL using a 100 kDa Amicon® spin concentrator (Millipore).

### Antibody-dependent cellular phagocytosis

Monocyte-mediated phagocytosis was measured with a bead-based assay and the THP-1 cell line, as previously described<sup>64</sup>. Briefly, biotinylated (EZ-Link Sulfo-NHS-LC-LC-Biotin, Thermo Fisher) BG505 SOSIP trimer was coupled to 1 μm yellow fluorescent neutravidin beads (Thermo Fisher) for 2 h at 37 °C. Excess antigen was removed in two washes with 0.1% BSA in PBS for blocking. Then, saturated beads (1.82 × 10<sup>8</sup> beads/well) were incubated with 10 μL of mAb (RM19R, VRC01, or PGT145 at various concentrations, starting at 5 μg/mL, 2-fold dilutions) in PBS for 2 h at 37 °C. ICs were washed and 2.5 × 10<sup>4</sup> THP-1 cells (American Type Culture Collection) were added per well and incubated for 16 h at 37 °C. Cells were fixed in 4% paraformaldehyde (PFA) and sample acquisition was performed via flow cytometry (IntelliCyt, iQue Screener plus). Events were gated on single cells and bead-positive cells. A phagocytosis score was calculated as the percent of bead-positive cells × GMFI/1000. All samples were run in duplicate.

### Measurement of FcγR binding via Luminex

A customized Luminex assay was used to quantify the relative FcγR binding as described previously<sup>65</sup>. Carboxyl-modified microspheres (Luminex) were coupled with BG505 SOSIP trimer. Coupling was performed by covalent *N*-hydroxysuccinimide (NHS)-ester linkages via EDC (Thermo Scientific) and Sulfo-NHS (Thermo Scientific) according to the manufacturer's instructions. Monoclonal antibodies were diluted starting at

5 µg/mL, 2-fold dilutions until 0.078 µg/mL, and 5 µL per sample was plated in duplicate. A total of  $1.2 \times 10^3$  beads per Luminex region per well were diluted in Luminex assay buffer containing 0.1% BSA and 0.05% Tween-20 and 45 µL of bead mix was added to each well of a 384-well plate (Greiner Bio-one). ICs were formed for 16 h at 4 °C on a rocking plate. The microspheres were washed three times with 60 µL of Luminex assay buffer with an automated plate washer (Tecan). Recombinant rhesus FcγRIIA-1, FcγRIIA-2, FcγRIIA-3, FcγRII-4, and FcγRIIA-1 (Duke Protein Production facility) were biotinylated (Thermo Scientific) and then conjugated to Streptavidin-PE (Southern Biotech) before the addition to ICs for 1 h. The antigen-coated Luminex beads were then washed and read on a cytometer (IntelliCyt, iQue Screener plus). Events were gated based on their bead fluorescence and the readout is PE MFI. Samples were run in duplicate per each secondary detection agent.

### Cryo-EM grid preparation

A Vitrobot mark IV (Thermo Fisher Scientific) was used for grid preparation for both the BG505 SOSIP/RM19R complex and BG505 SOSIP-T33\_dn2 nanoparticle samples. Temperature was set to 10 °C, humidity at 100% with a 4–7 s blotting time, blotting force of 0, and wait time of 10 s. For the RM19R sample, 3 µL of the BG505 SOSIP/RM19R complex at 13 mg/mL was mixed with 1 µL of a *n*-dodecyl-β-D-maltopyranoside (DDM) solution to a final DDM concentration of 0.06 mM and applied to a C-Flat grid (CF-2/2-4C, Protochips Inc.), which had been plasma-cleaned for 5 s using a mixture of Ar/O<sub>2</sub> (Gatan Solarus 950 Plasma system). For the BG505 SOSIP-T33\_dn2 nanoparticle sample, lauryl maltose neopentyl glycol at a final concentration of 0.005 mM was added to the nanoparticle sample (4.0 mg/mL) and 3 µL was immediately loaded onto plasma-cleaned Quantifoil R 2/1 holey carbon copper grid (Cu, 400-mesh, Quantifoil Micro Tools GmbH). Blotted grids were plunge frozen into nitrogen-cooled liquid ethane.

### Cryo-EM data collection and processing

Samples were imaged on either FEI Titan Krios electron microscope (Thermo Fisher) operating at 300 keV (RM19R dataset) or a FEI Talos Arctica electron microscope (Thermo Fisher) operating at 200 keV (T33\_dn2 nanoparticle datasets). Both microscopes were equipped with Gatan K2 Summit direct electron detectors operating in counting mode. Automated data collection was performed using the Legion software suite<sup>62</sup>. Micrograph movie frames were aligned and dose-weighted using MotionCor2<sup>66</sup>, and CTF models were determined using Gctf<sup>67</sup>. For the RM19R dataset, dose-weighted micrographs were assessed using EMHP<sup>68</sup> and particles were picked using DoG Picker<sup>69</sup>. Particle extraction, 2D classification, and 3D refinement were conducted using Relion v2.1<sup>70</sup>. For the T33\_dn2 nanoparticle, three datasets were collected and initial data processing was performed in cryoSPARC v2.5.0<sup>71</sup>. Particles were picked using cryoSPARC template picker, extracted and 2D classified. Particles belonging to nanoparticle classes (89,863) were then transferred to Relion/3.0<sup>63</sup> for further processing. A reference model was generated using Ab-Initio Reconstruction in cryoSPARC. Several iterative 3D refinement and classification steps in Relion were applied to identify a subpopulation of 35,521 particles that went into the final 3D reconstructions. Tetrahedral symmetry was applied for all 3D steps. Soft solvent mask around the nanoparticle core was introduced during the final 3D classification, refinement, and post-processing steps. Final resolution of the NP core was 4.6 Å after post-processing. Trimeric BG505 SOSIP antigens were connected to the nanoparticle core via a flexible linker and they appeared disordered in the final map of the nanoparticle. In order to obtain high-resolution information on the BG505 SOSIP trimers, we applied localized reconstruction v1.2.0<sup>72</sup>. First, marker files were generated in UCSF Chimera<sup>73</sup> to define the subparticle vectors. Then, the trimer subparticles were extracted from aligned nanoparticles from which the signal corresponding to the nanoparticle core has been subtracted. Each nanoparticle displayed four trimers, so the total number of extracted subparticles was 142,084 ( $4 \times 35,521$ ). Trimer subparticles were then 2D and 3D classified in Relion. A subset of 52,939 subparticles was subjected to 3D auto-refinement with C3 symmetry. Soft solvent mask was applied during refinement and post-processing steps. Final resolution of the presented BG505 SOSIP antigen map is 4.5 Å. A graphical summary of the data processing approach and relevant statistics are displayed in Supplementary Fig. 1a. Data collection and processing parameters are reported in Supplementary Table 1.

### Model building and refinement

A model of the Fv region of RM19R was generated using the Rosetta antibody protocol available on the ROSIE server<sup>74,75</sup>. An initial molecular model of the BG505 SOSIP trimer/RM19R Fab complexes was built by docking the Env portion of PDB: 5ACO<sup>76</sup> into the EM density maps along with the RM19R Fv model generated in Rosetta using UCSF Chimera<sup>73</sup>. The appropriate mutations were introduced into the Env sequence to match the BG505 SOSIP.v5.2.N241.N289 sequence and N-linked glycans were added using Coot<sup>77</sup>. Initial models for T33\_dn2 nanoparticle core and the BG505 SOSIP trimer were relaxed into the post-processed, *B*-factor sharpened maps following 3D refinement. For all models, iterative rounds of Rosetta relaxed refinement<sup>78,79</sup> and manual refinement in Coot<sup>77</sup> were used to generate the final models. Appropriate symmetry (tetrahedral for NP and C3 for BG505 SOSIP trimer and BG505 SOSIP/RM19R Fab complex) was applied during the automated refinement steps. EMRinger and MolProbity scores were used for assessment of refined models<sup>80,81</sup>. Glycan structures were validated by CARP<sup>82</sup>, pdb-care<sup>83</sup>, and Privateer<sup>84</sup>. Final model statistics are summarized in Supplementary Table II.

### Immunizations

**Animals.** All relevant ethical regulations for animal testing and research have been followed.

Female BALB/c mice 8 weeks of age were purchased from Jackson Laboratories, housed at the Koch Institute for Integrative Cancer Research, and maintained in accordance with NIH guidelines. This study was approved by the MIT Institutional Animal Care and Use Committee (IACUC).

Indian rhesus macaques (*Macaca mulatta*) (RM) were housed at the Yerkes National Primate Research Center and maintained in accordance with NIH guidelines. This study was approved by the Emory University IACUC. All animals were treated with anesthesia and analgesics for procedures as per veterinarian recommendations and IACUC-approved protocol.

**Adjuvant.** The adjuvant used for all immunizations was an ISCOM-like nanoparticle comprised of self-assembled cholesterol, phospholipid, and Quilaja saponin prepared as previously described<sup>85</sup>.

**IC studies.** Groups of three mice were injected i.v. with RM19R mAb at 10 or 1 mg/kg or an equivalent volume of PBS. After 24 h, all animals received s.c. injections on each side of the spine at the tail base of 2.5 µg BG505 SOSIP trimer immunogen combined with 2.5 µg saponin adjuvant (5 µg of each total per mouse). At 1, 3, or 7 days after antigen injection, animals were sacrificed and the inguinal LNs were removed and fixed for imaging by flatbed fluorescence scanner, as described below. In a separate experiment, another group of mice was dosed i.v. with 0.25 mg/kg RM19R mAb prior to the subcutaneous administration of immunogen and trimer as above. The LNs from this experiment were used for confocal microscopy.

For the analogous RM study, pairs of RM were injected i.v. with 1:1 mixtures of fluorescently labeled and unlabeled RM19R mAb at 2.0 or 0.2 mg/kg, and 24 h later, all animals received s.c. injections in each thigh of 50 µg BG505 SOSIP trimer immunogen combined with 187.5 µg saponin adjuvant; a control group received SOSIP trimer and adjuvant in the absence of RM19R passive transfer. At 3 days after antigen injection, animals were sacrificed and all LNs in selected locations were collected for analysis.

**Nanoparticle immunogen study.** Groups of three RM were immunized on day 0 with 50 µg BG505 SOSIP MD39 trimer<sup>9</sup> or 71 µg BG505 SOSIP-T33\_dn2 nanoparticle (to achieve an equimolar dose on a per-trimer basis) conjugated to Alexa Fluor 647 s.c. in both left and right inner mid thighs combined with 187.5 µg of saponin adjuvant. Animals were sacrificed 2 or 7 days after immunization and all LNs in selected locations were collected for analysis.

### Ex vivo tissue fixation

All LNs were harvested and immediately placed in PLP buffer (pH 7.4 50 mM PBS + 100 mM lysine, 1% PFA, 2 mg/mL sodium periodate) for fixation. After incubation at 4 °C overnight for mouse LNs or 4–5 days for RM LNs, the tissues were washed and stored in PBS with 0.05% sodium azide at 4 °C until taken for imaging.

### Whole-organ fluorescence measurement

Total antigen signal within LNs from the antigen tracking study was measured in two ways. First, by IVIS (PerkinElmer) fluorescence imaging of whole tissues within clear plastic 24-well plates, using excitation at 570 nm and emission at 620 nm (for trimer-AF568) and excitation at 640 nm and emission at 680 nm (for RM19R-AF647). Alternatively, fluorescence was measured by placing the tissues directly on the glass scanning surface of a Typhoon FLA 9500 biomolecular imager (GE Healthcare Life Sciences) and using either a 535-nm excitation laser with a >575-nm long-pass filter, or a 635-nm excitation laser and a ≥665-nm long-pass filter. The integrated signal density corresponding to labeled antigen or antibody in each LN was calculated using LivingImage (PerkinElmer) or ImageJ software and plotted using GraphPad Prism 8. For comparing trimer to nanoparticle in Fig. 5b, the difference in degree of labeling between soluble trimer and the nanoparticle was used to normalize the signal on a per-trimer basis.

### Whole-organ clarification

Selected LNs were clarified via a combination/modification of the iDISCO<sup>40</sup> and CUBIC<sup>41</sup> organ-clearing methods. The LNs were first delipidated based on the iDISCO methanol incubation protocol: tissues were washed in water for 1 h and then 20% methanol in water for 2 h. A series of stepwise increases in methanol percentage (40%, 60%, 100%, and 100%) followed, each step for 2 h. The LNs were then placed into 2:1 MeOH:DCM overnight, and the next day were rehydrated with the following series of methanol solutions for 2 h each: 100%, 100%, 80%, 60%, 40%, 20%, 0%, and 0%. Next, the LNs were placed into 10–20 mL of a 1:1 mixture of CUBIC-R index-matching solution (45 wt% antipyrine and 30 wt% nicotinamide in water) for 1 day, followed by at least 20 mL of undiluted CUBIC-R for 2 days or as long as needed for adequate clarification. Larger organs were moved into a fresh 20 mL of CUBIC-R solution to ensure that the refractive index of the solution would not be significantly lowered by residual water in the tissue.

### Light sheet microscopy

Clarified LNs were imaged in CUBIC-R solution using a LaVision Ultramicroscope II Light Sheet Microscope at ×1.25 optical zoom. The Alexa Fluor 647-labeled antigen or antibody was imaged using the 640-nm laser, and the Alexa Fluor 568-labeled antigen was imaged using the 561-nm laser at 100 ms exposure time on an Andor Neo camera. Snapshots and movies were generated using the 3D viewer in the FIJI package of ImageJ. Follicles containing fluorescently labeled antigen were counted manually using the maximum projection of each LN.

### Immunofluorescence staining

Mouse LNs were blocked and permeabilized overnight in PBS with 5% mouse serum, 5% rat serum, and 0.2% Triton X-100, followed by staining for 3 days at 37 °C with 1:100 dilutions of BV421-labeled rat anti-mouse CD35 clone 8C12 (BD Biosciences) and Alexa Fluor 488-labeled mouse anti-Ki67 clone B56 (BD Biosciences) in the same buffer as the blocking/permeabilization step. Stained LNs were then washed for 3 days at room temperature with PBS containing 0.2% Tween-20 and then the fixation protocol was repeated prior to whole-organ clarification.

Selected RM LNs were embedded in 3% low melting temperature agarose (Sigma-Aldrich) and then sliced into 100- or 350-µm-thick sections using a vibratome. The slices were blocked and permeabilized overnight in PBS with 5% mouse serum, 5% rat serum, and 0.2% Triton X-100, followed by staining for 3 days at 37 °C with 1:100 dilutions of BV421-labeled mouse anti-human CD35 clone E11 (BD Biosciences) and Alexa Fluor 488-labeled mouse anti-Ki67 clone B56 (BD Biosciences) in the same buffer as the blocking/permeabilization step. Stained slices were then washed for 3 days at room temperature with PBS containing 0.2% Tween-20 and then mounted onto glass slides with Prolong Glass antifade mountant (Thermo Fisher Scientific).

### Confocal microscopy

Imaging was performed on either one of a Leica SP8 or an Olympus FV1200 laser scanning confocal microscope using ×10 air or ×20 water immersion objectives. Lasers were set to minimize pixel saturation in the brightest samples. All laser and channel settings were then kept constant across timepoints for individual studies to allow for direct comparison between different samples. The 50- to 100-µm-thick z-stacks were collected by imaging with a z-step size of 5 µm. Images were analyzed using ImageJ, and single planes were selected for figures based on how

well they represented the antigen spread within follicles or the tissue as a whole.

### Binding experiments with MBL

Truncated human MBL-2 was purchased from MyBioSource (Cat# MBS2086086). Five micrograms of MBL-2 was incubated with 5 µg of BG505 SOSIP or BG505 SOSIP-T33\_dn2 nanoparticle for 4 h at 37 °C in TBS buffer (Alfa Aesar) containing 2 mM CaCl<sub>2</sub>. Following incubation, the samples were diluted to 40 µg/mL, loaded onto carbon-coated copper EM grids, negatively stained with uranyl-formate, and imaged as described in the “Negative stain-electron microscopy” section. Imaging was also performed on grids containing free, noncomplexed MBL-2, BG505 SOSIP, and BG505 SOSIP-T33\_dn2 NP for comparison. For SEC experiments, 30 µg of MBL-2 was mixed with 15 µg of BG505 SOSIP or BG505 SOSIP-T33\_dn2 nanoparticle samples and incubated for 4 h at 37 °C in TBS + 2 mM CaCl<sub>2</sub>. For comparison, equivalent amounts of free MBL-2, BG505 SOSIP, and BG505 SOSIP-T33\_dn2 nanoparticle were incubated under identical conditions. For the SEC step, we used a Superose 6 Increase 10/300 column, running in TBS + 2 mM CaCl<sub>2</sub>. SEC traces of the assembly and control reactions are shown in Supplementary Fig. 4b, c.

### Reporting summary

Further information on research design is available in the Nature Research Reporting Summary linked to this article.

### DATA AVAILABILITY

Cryo-EM reconstructions have been deposited in the Electron Microscopy Data Bank (EMDB: EMD-21227, EMD-21230, and EMD-21231), and in the Protein Data Bank (PDB: 6VKN, 6VL5, and 6VL6). All other data from the current study are available from the corresponding authors on reasonable request.

Received: 17 February 2020; Accepted: 11 June 2020;

Published online: 05 August 2020

### REFERENCES

- Haynes, B. F. & Burton, D. R. Developing an HIV vaccine. *Science* **355**, 1129–1130 (2017).
- Kwong, P. D. & Mascola, J. R. HIV-1 vaccines based on antibody identification, B cell ontogeny, and epitope structure. *Immunity* **48**, 855–871 (2018).
- Pauthner, M. et al. Elicitation of robust tier 2 neutralizing antibody responses in nonhuman primates by HIV envelope trimer immunization using optimized approaches. *Immunity* **46**, 1073–1088. e1076 (2017).
- Sanders, R. W. et al. HIV-1 VACCINES. HIV-1 neutralizing antibodies induced by native-like envelope trimers. *Science* **349**, aac4223 (2015).
- Lyumkisi, D. et al. Cryo-EM structure of a fully glycosylated soluble cleaved HIV-1 envelope trimer. *Science* **342**, 1484–1490 (2013).
- Julien, J. P. et al. Crystal structure of a soluble cleaved HIV-1 envelope trimer. *Science* **342**, 1477–1483 (2013).
- Sanders, R. W. et al. A next-generation cleaved, soluble HIV-1 Env trimer, BG505 SOSIP.664 gp140, expresses multiple epitopes for broadly neutralizing but not non-neutralizing antibodies. *PLoS Pathog.* **9**, e1003618 (2013).
- Escolano, A. et al. Immunization expands B cells specific to HIV-1 V3 glycan in mice and macaques. *Nature* **570**, 468–473 (2019).
- Steichen, J. M. et al. HIV vaccine design to target germline precursors of glycan-dependent broadly neutralizing antibodies. *Immunity* **45**, 483–496 (2016).
- Chuang, G. Y. et al. structure-based design of a soluble prefusion-closed HIV-1 Env Trimer with reduced CD4 affinity and improved immunogenicity. *J. Virol.* **91**, <https://doi.org/10.1128/JVI.02268-16> (2017).
- Gitlin, A. D. et al. HUMORAL IMMUNITY. T cell help controls the speed of the cell cycle in germinal center B cells. *Science* **349**, 643–646 (2015).
- Shulman, Z. et al. Dynamic signaling by T follicular helper cells during germinal center B cell selection. *Science* **345**, 1058–1062 (2014).
- Liu, D. et al. T–B-cell entanglement and ICOSL-driven feed-forward regulation of germinal center reaction. *Nature* **517**, 214–218 (2015).
- Carroll, M. C. & Iseman, D. E. Regulation of humoral immunity by complement. *Immunity* **37**, 199–207 (2012).
- Jayasekera, J. P., Moseman, E. A. & Carroll, M. C. Natural antibody and complement mediate neutralization of influenza virus in the absence of prior immunity. *J. Virol.* **81**, 3487–3494 (2007).

16. Junt, T. et al. Subcapsular sinus macrophages in lymph nodes clear lymph-borne viruses and present them to antiviral B cells. *Nature* **450**, 110–114 (2007).
17. Phan, T. G., Grigorova, I., Okada, T. & Cyster, J. G. Subcapsular encounter and complement-dependent transport of immune complexes by lymph node B cells. *Nat. Immunol.* **8**, 992–1000 (2007).
18. Carrasco, Y. R. & Batista, F. D. B cells acquire particulate antigen in a macrophage-rich area at the boundary between the follicle and the subcapsular sinus of the lymph node. *Immunity* **27**, 160–171 (2007).
19. Heesters, B. A. et al. Endocytosis and recycling of immune complexes by follicular dendritic cells enhances B cell antigen binding and activation. *Immunity* **38**, 1164–1175 (2013).
20. Park, C., Arthos, J., Cicala, C. & Kehrl, J. H. The HIV-1 envelope protein gp120 is captured and displayed for B cell recognition by SIGN-R1(+) lymph node macrophages. *eLife* **4**, <https://doi.org/10.7554/eLife.06467> (2015).
21. Frank, M. M., Hester, C. & Jiang, H. Complement and the control of HIV infection: an evolving story. *Curr. Opin. HIV AIDS* **9**, 278–290 (2014).
22. Nutt, S. L., Hodgkin, P. D., Tarlinton, D. M. & Corcoran, L. M. The generation of antibody-secreting plasma cells. *Nat. Rev. Immunol.* **15**, 160–171 (2015).
23. Cirelli, K. M. & Crotty, S. Germinal center enhancement by extended antigen availability. *Curr. Opin. Immunol.* **47**, 64–69 (2017).
24. Dempsey, P. W., Allison, M. E., Akkaraju, S., Goodnow, C. C. & Fearon, D. T. C3d of complement as a molecular adjuvant: bridging innate and acquired immunity. *Science* **271**, 348–350 (1996).
25. Hioe, C. E. et al. Modulation of antibody responses to the V1V2 and V3 regions of HIV-1 envelope by immune complex vaccines. *Front. Immunol.* **9**, 2441 (2018).
26. Kumar, R. et al. Elicitation of broadly reactive antibodies against glycan-modulated neutralizing V3 epitopes of HIV-1 by immune complex vaccines. *Vaccine* **31**, 5413–5421 (2013).
27. Gach, J. S. et al. Antibody responses elicited by immunization with BG505 trimer immune complexes. *J. Virol.* **93**, <https://doi.org/10.1128/JVI.01188-19> (2019).
28. Chen, Y. et al. An HIV-1 Env-antibody complex focuses antibody responses to conserved neutralizing epitopes. *J. Immunol.* **197**, 3982–3998 (2016).
29. Diamos, A. G. et al. Vaccine synergy with virus-like particle and immune complex platform for delivery of human papillomavirus L2 antigen. *Vaccine* **37**, 137–144 (2019).
30. Phoolcharoen, W. et al. A nonreplicating subunit vaccine protects mice against lethal Ebola virus challenge. *Proc. Natl Acad. Sci. USA* **108**, 20695–20700 (2011).
31. Xu, D. Z. et al. Results of a phase III clinical trial with an HBsAg-HBIG immunogenic complex therapeutic vaccine for chronic hepatitis B patients: experiences and findings. *J. Hepatol.* **59**, 450–456 (2013).
32. Xu, D. Z. et al. A randomized controlled phase IIb trial of antigen-antibody immunogenic complex therapeutic vaccine in chronic hepatitis B patients. *PLoS ONE* **3**, e2565 (2008).
33. Mendoza, P. et al. Combination therapy with anti-HIV-1 antibodies maintains viral suppression. *Nature* **561**, 479–484 (2018).
34. Scheid, J. F. et al. HIV-1 antibody 3BNC117 suppresses viral rebound in humans during treatment interruption. *Nature* **535**, 556–560 (2016).
35. Lynch, R. M. et al. Virologic effects of broadly neutralizing antibody VRC01 administration during chronic HIV-1 infection. *Sci. Transl. Med.* **7**, 319ra206 (2015).
36. Tokatlian, T. et al. Innate immune recognition of glycans targets HIV nanoparticle immunogens to germinal centers. *Science* **363**, 649–654 (2019).
37. Ueda, G. et al. Tailored design of protein nanoparticle scaffolds for multivalent presentation of viral glycoprotein antigens. Preprint at <https://doi.org/10.1101/2020.01.29.923862> (2020).
38. Antanasijevic, A. et al. Structural and functional evaluation of de novo-designed, two-component nanoparticle carriers for HIV Env trimer immunogens. Preprint at <https://doi.org/10.1101/2020.01.31.929273> (2020).
39. Cottrell, C. A. et al. Mapping the immunogenic landscape of near-native HIV-1 envelope trimers in non-human primates. Preprint at <https://doi.org/10.1101/2020.02.05.936096> (2020).
40. Renier, N. et al. Mapping of brain activity by automated volume analysis of immediate early genes. *Cell* **165**, 1789–1802 (2016).
41. Kubota, S. I. et al. Whole-body profiling of cancer metastasis with single-cell resolution. *Cell Rep.* **20**, 236–250 (2017).
42. Brouwer, P. J. M. et al. Enhancing and shaping the immunogenicity of native-like HIV-1 envelope trimers with a two-component protein nanoparticle. *Nat. Commun.* **10**, 4272 (2019).
43. Marcandalli, J. et al. Induction of potent neutralizing antibody responses by a designed protein nanoparticle vaccine for respiratory syncytial virus. *Cell* **176**, 1420–1431. e1417 (2019).
44. Catron, D. M., Pape, K. A., Fife, B. T., van Rooijen, N. & Jenkins, M. K. A protease-dependent mechanism for initiating T-dependent B cell responses to large particulate antigens. *J. Immunol.* **184**, 3609–3617 (2010).
45. Kulp, D. W. et al. Structure-based design of native-like HIV-1 envelope trimers to silence non-neutralizing epitopes and eliminate CD4 binding. *Nat. Commun.* **8**, 1655 (2017).
46. Cirelli, K. M. et al. Slow delivery immunization enhances HIV neutralizing antibody and germinal center responses via modulation of immunodominance. *Cell* **177**, 1153–1171. e1128 (2019).
47. Tam, H. H. et al. Sustained antigen availability during germinal center initiation enhances antibody responses to vaccination. *Proc. Natl Acad. Sci. USA* **113**, E6639–E6648 (2016).
48. Berzofsky, J. A. et al. Antigenic peptides recognized by T lymphocytes from AIDS viral envelope-immune humans. *Nature* **334**, 706–708 (1988).
49. Bianchi, M. et al. Electron-microscopy-based epitope mapping defines specificities of polyclonal antibodies elicited during HIV-1 BG505 envelope trimer immunization. *Immunity* **49**, 288–300. e288 (2018).
50. Hu, J. K. et al. Murine antibody responses to cleaved soluble HIV-1 envelope trimers are highly restricted in specificity. *J. Virol.* <https://doi.org/10.1128/JVI.01653-15> (2015).
51. Cheng, C. et al. Immunogenicity of a prefusion HIV-1 envelope trimer in complex with a quaternary-structure-specific antibody. *J. Virol.* **90**, 2740–2755 (2015).
52. Link, A. et al. Innate immunity mediates follicular transport of particulate but not soluble protein antigen. *J. Immunol.* **188**, 3724–3733 (2012).
53. Ols, S. et al. Route of vaccine administration alters antigen trafficking but not innate or adaptive immunity. *Cell Rep.* **30**, 3964–3971. e3967 (2020).
54. Ingale, J. et al. High-density array of well-ordered HIV-1 spikes on synthetic liposomal nanoparticles efficiently activate B cells. *Cell Rep.* **15**, 1986–1999 (2016).
55. Sliopen, K. et al. Presenting native-like HIV-1 envelope trimers on ferritin nanoparticles improves their immunogenicity. *Retrovirology* **12**, 82 (2015).
56. Jardine, J. G. et al. HIV-1 VACCINES. Priming a broadly neutralizing antibody response to HIV-1 using a germline-targeting immunogen. *Science* **349**, 156–161 (2015).
57. Torrents de la Pena, A. et al. Improving the Immunogenicity of native-like HIV-1 envelope trimers by hyperstabilization. *Cell Rep.* **20**, 1805–1817 (2017).
58. Walker, L. M. et al. Broad neutralization coverage of HIV by multiple highly potent antibodies. *Nature* **477**, 466–470 (2011).
59. Wu, X. et al. Rational design of envelope identifies broadly neutralizing human monoclonal antibodies to HIV-1. *Science* **329**, 856–861 (2010).
60. Lee, J. H. et al. Antibodies to a conformational epitope on gp41 neutralize HIV-1 by destabilizing the Env spike. *Nat. Commun.* **6**, 8167 (2015).
61. Ozorowski, G. et al. Effects of adjuvants on HIV-1 envelope glycoprotein SOSIP trimers in vitro. *J. Virol.* **92**, <https://doi.org/10.1128/JVI.00381-18> (2018).
62. Suloway, C. et al. Automated molecular microscopy: the new Legimon system. *J. Struct. Biol.* **151**, 41–60 (2005).
63. Zivanov, J. et al. New tools for automated high-resolution cryo-EM structure determination in RELION-3. *Elife* **7**, <https://doi.org/10.7554/eLife.42166> (2018).
64. Ackerman, M. E. et al. A robust, high-throughput assay to determine the phagocytic activity of clinical antibody samples. *J. Immunol. Methods* **366**, 8–19 (2011).
65. Brown, E. P. et al. High-throughput, multiplexed IgG subclassing of antigen-specific antibodies from clinical samples. *J. Immunol. Methods* **386**, 117–123 (2012).
66. Zheng, S. Q. et al. MotionCor2: anisotropic correction of beam-induced motion for improved cryo-electron microscopy. *Nat. Methods* **14**, 331–332 (2017).
67. Zhang, K. Gctf: Real-time CTF determination and correction. *J. Struct. Biol.* **193**, 1–12 (2016).
68. Berndsen, Z., Bowman, C., Jang, H. & Ward, A. B. EMHP: an accurate automated hole masking algorithm for single-particle cryo-EM image processing. *Bioinformatics* **33**, 3824–3826 (2017).
69. Voss, N. R., Yoshioka, C. K., Radermacher, M., Potter, C. S. & Carragher, B. DoG Picker and TiltPicker: software tools to facilitate particle selection in single particle electron microscopy. *J. Struct. Biol.* **166**, 205–213 (2009).
70. Kimanius, D., Forsberg, B. O., Scheres, S. H. & Lindahl, E. Accelerated cryo-EM structure determination with parallelisation using GPUs in RELION-2. *Elife* **5**, <https://doi.org/10.7554/eLife.18722> (2016).
71. Punjani, A., Rubinstein, J. L., Fleet, D. J. & Brubaker, M. A. cryoSPARC: algorithms for rapid unsupervised cryo-EM structure determination. *Nat. Methods* **14**, 290–296 (2017).
72. Ilca, S. L. et al. Localized reconstruction of subunits from electron cryomicroscopy images of macromolecular complexes. *Nat. Commun.* **6**, 8843 (2015).
73. Pettersen, E. F. et al. UCSF Chimera—a visualization system for exploratory research and analysis. *J. Comput. Chem.* **25**, 1605–1612 (2004).
74. Lyskov, S. et al. Serverification of molecular modeling applications: the Rosetta Online Server that Includes Everyone (ROSIE). *PLoS ONE* **8**, e63906 (2013).
75. Weitzner, B. D. et al. Modeling and docking of antibody structures with Rosetta. *Nat. Protoc.* **12**, 401–416 (2017).
76. Lee, J. H., de Val, N., Lyumkis, D. & Ward, A. B. Model building and refinement of a natively glycosylated HIV-1 Env protein by high-resolution cryoelectron microscopy. *Structure* **23**, 1943–1951 (2015).
77. Casanal, A., Lohkamp, B. & Emsley, P. Current developments in coot for macromolecular model building of electron cryo-microscopy and crystallographic data. *Protein Sci.* <https://doi.org/10.1002/pro.3791> (2019).

78. DiMaio, F., Tyka, M. D., Baker, M. L., Chiu, W. & Baker, D. Refinement of protein structures into low-resolution density maps using rosetta. *J. Mol. Biol.* **392**, 181–190 (2009).
79. Frenz, B. et al. Automatically fixing errors in glycoprotein structures with Rosetta. *Structure* **27**, 134–139. e133 (2019).
80. Barad, B. A. et al. EMRinger: side chain-directed model and map validation for 3D cryo-electron microscopy. *Nat. Methods* **12**, 943–946 (2015).
81. Williams, C. J. et al. MolProbity: more and better reference data for improved all-atom structure validation. *Protein Sci.* **27**, 293–315 (2018).
82. Lutteke, T., Frank, M. & von der Lieth, C. W. Carbohydrate Structure Suite (CSS): analysis of carbohydrate 3D structures derived from the PDB. *Nucleic Acids Res.* **33**, D242–D246 (2005).
83. Lutteke, T. & von der Lieth, C. W. pdb-care (PDB carbohydrate residue check): a program to support annotation of complex carbohydrate structures in PDB files. *BMC Bioinform.* **5**, 69 (2004).
84. Agirre, J. et al. Privateer: software for the conformational validation of carbohydrate structures. *Nat. Struct. Mol. Biol.* **22**, 833–834 (2015).
85. Lövgren-Bengtsson, K. & Morein, B. in *Vaccine Adjuvants: Preparation Methods and Research Protocols* (ed. O'Hagan, D.) 239–258 (Humana Press, Totowa, 2000).

## ACKNOWLEDGEMENTS

We thank Jean-Christophe Ducom, Hannah L. Turner, Bill Anderson, and Charles Bowman for assistance with computational resources, microscope management, and data collection. This work was supported in part by the NIH (awards UM1AI100663 and UM1AI144462 to D.J.I., S.C., W.R.S., G.S., and A.B.W., AI125068 to D.J.I., S.C., and G.S., and P01AI048240 to D.J.I., and NINDS P30 Core Center Grant #NS072030), the Bill & Melinda Gates Foundation (OPP1156262 to D.B. and N.P.K.), the Ragon Institute for MGH, MIT, and Harvard, and the Samana Cay MGH Research Scholars 2017–2022 program (G.A.). C.A.C. is supported by the NIH F31 Ruth L. Kirschstein Predoctoral Award AI131873 and by the Achievement Rewards for College Scientists Foundation. The content is solely the responsibility of the authors and does not necessarily represent the official views of the National Institutes of Health. D.B. and D.J.I. are investigators of the Howard Hughes Medical Institute.

## AUTHOR CONTRIBUTIONS

A.B.W., S.C., D.J.I., J.T.M., K.M.C., A.A., and C.A.C. conceived the study plan. J.T.M. performed the mouse experiments. J.T.M. and B.J.C. produced fluorophore-labeled BG505 SOSIP and performed all fluorescent imaging experiments. C.A.C. produced and characterized RM19R, fluorophore-labeled RM19R, and performed ELISAs. A.A. and J.C. produced, characterized, and fluorophore labeled the T33\_dn2 nanoparticle, and carried out MBL binding studies. G.U., N.P.K., and D.B. designed the T33\_dn2 nanoparticle. T.T. produced the ISCOM-like adjuvant. D.G.C., C.A.E., E.H.G, Y.C., F.V., and G.S. performed the NHP immunizations and tissue collection. T.S., S.M., and W.R.S.

provided the BG505 SOSIP trimer used in the nanoparticle comparison study. S.F. and G.A. performed the ADCP and FcγR interaction assays for the RM19R Ab. J.T.M., C.A.C., A.A., A.B.W., and D.J.I. wrote the manuscript. A.B.W., G.S., and D.J.I. supervised the study.

## COMPETING INTERESTS

D.B. and G.U. are inventors on US patent application 62/422,872 titled “Computational design of self-assembling cyclic protein homo-oligomers”. D.B., N.P.K., and G.U. are inventors on US patent application 62/636,757 titled “Method of multivalent antigen presentation on designed protein nanomaterials”. N.P.K. and D.B. are co-founders and shareholders in Icosavax, a company that has licensed these patent applications, and N.P.K. is a member of Icosavax’s Scientific Advisory Board. All other authors declare no competing interests.

## ADDITIONAL INFORMATION

**Supplementary information** is available for this paper at <https://doi.org/10.1038/s41541-020-00223-1>.

**Correspondence** and requests for materials should be addressed to A.B.W. or D.J.I.

**Reprints and permission information** is available at <http://www.nature.com/reprints>

**Publisher’s note** Springer Nature remains neutral with regard to jurisdictional claims in published maps and institutional affiliations.



**Open Access** This article is licensed under a Creative Commons Attribution 4.0 International License, which permits use, sharing, adaptation, distribution and reproduction in any medium or format, as long as you give appropriate credit to the original author(s) and the source, provide a link to the Creative Commons license, and indicate if changes were made. The images or other third party material in this article are included in the article’s Creative Commons license, unless indicated otherwise in a credit line to the material. If material is not included in the article’s Creative Commons license and your intended use is not permitted by statutory regulation or exceeds the permitted use, you will need to obtain permission directly from the copyright holder. To view a copy of this license, visit <http://creativecommons.org/licenses/by/4.0/>.

© The Author(s) 2020